UNIVERSIDAD DE VALPARAÍSO

FACULTAD DE CIENCIAS

PROGRAMA DE MAGISTER EN CIENCIAS BIOLÓGICAS

MENCIÓN NEUROCIENCIAS

STRUCTURE-FUNCTION RELATIONSHIP IN BIOPHYSICALLY INSPIRED SMALL WORLD NETWORKS

JAVIER EDUARDO PALMA ESPINOSA

TUTOR
DR. PATRICIO ORIO

Proyecto de Tesis para optar al grado de Magister en Ciencias

VALPARAÍSO – CHILE
2021

Hey man of science with your perfect rules of measurement

Can you improve this place with the data that you gather?. . .

Bad Religion

ABSTRACT

How behavior arises from the neural activity observed in the brain is one of the main questions in neuroscience. In the resting state, synchronized and highly stable activity has been found in coordinated brain areas, forming what is known as Functional Connectivity. These brain areas are neuronal structures that are interconnected in a very particular way, generating a physical network known as Structural Connectivity. This connectivity has been studied in the light of complex networks, as it has been observed that the particular properties of the brain structure are related to small-world network topology. Interestingly, studies on Functional Connectivity have also proposed similar topology. Functional connectivity is not static, instead, it transits or "wanders" between several states of activity, which are constantly revisited. This dynamical wonder has been framed as the Functional Connectivity Dynamics. However, the relationship between this dynamic transit of Functional Connectivity and the structural basis on which it is supported remains unknown. In this work, the relationship between Structural Connectivity and Functional Connectivity Dynamics is explored by using three network topologies with a biophysically inspired model of activity. Small world metrics, integration, and segregation metrics were used for characterizing the structural connectivity, while multistability, metastability, and synchrony were used for characterizing functional connectivity dynamics. Metastability or "wandering" between activity patterns was higher in regular networks, and it diminished in small-world networks. The relationship between the segregation properties of the network explains better this observed behavior. Multistability, defined by the transit between multiples attractors, was also high in regular networks, however, the relationship between structural and dynamic was better explained by small world metrics. These analyses suggest that the dynamical richness may be originated due to the segregation properties of the network, but the transit between those states is imposed by the ratio between segregation and integration. Further analysis within the range of small-world, may help to understand the importance of this ratio in the dynamical analysis of the brain activity.

Contents

Chapter 1

Introduction

Brain activity is considered the main component that drives behavior in living organisms (Fox et al., 2007). Establishing a causal link between activity and behavior has been a major task in neuroscience. In the last decades, better imaging techniques and computational power have increased the studies focusing on the explanation of that link (Mill et al., 2017).

In the brain, each anatomic region has its own dynamic electrical activity, which may be observed through clinical measurements such as Electroencephalography(EEG), functional Magnetic Resonance Imaging (fMRI), Magnetoencephalography (MEG) among others (see da Silva (2013) for a review on M/EEG or Van Den Heuvel and Pol (2010) for fMRI). Studies on the correlation between these signals have revealed significant relationships between brain regions. For example, in fMRI experiments, when the subject is not engaged in any activity, blood oxygen level dependence (BOLD) signal decomposition reveals several modular networks, which have been related with different cognitive tasks (Park and Friston, 2013). These subnetworks account for highly stable and synchronized activity in certain brain areas and constitute what is known as Functional Connectivity (FC).

In the last years, the assumption of a stationary FC has retreated in the light of new experiments and observations, which show that the resting FC varies in time, transiting between a number of “states” with spatio-temporal characteristics, defining a particular dynamic termed Functional Connectivity Dynamics (FCD).

Functional connectivity dynamics (FCD) is defined as “ a manifestation of the self-organized activity of cortical networks, in which noise-driven fluctuations far from equilibrium lead to the stochastic sampling of a rich repertoire of characteristic system’s trajectories” (Hansen et al., 2015). In other words, changes in the activity of cortical networks generate changes in the overall system’s dynamic, allowing it to visit or re-visit particular “states”. The nature of these changes has been studied intensively in the local scale (cortical areas), or mesoscale (coupling between

areas), proposing mechanisms that could explain the observed FCD.

At the local scale, changes in the dynamics of cortical areas (or nodes in computational models) have been proposed as a mechanism that could explain the FCD. For example, neural noise, generated by stochastic opening and closing of ionic channels, moves the stable operating point of brain activity to another one, allowing the system to explore different stable points (Berglund and Gentz, 2010; Heitmann and Breakspear, 2018). This mechanism has been reported as a key element in the emergence of brain states reported in FCD (Orio et al., 2018).

On the other hand, chaotic behavior in brain activity is also related to “dynamical wandering” between states. In this type of dynamic regime, chaos acts also as a promoter of what is known as multistable behavior, allowing the system to visit other stable or quasi-stable states(Xu et al., 2018). Finally, structural coupling between subnetworks has also shown to drive FCD(Heitmann and Breakspear, 2018), by imposing an oscillatory regime derived by the interconnections within brain areas(Cabral et al., 2014; Orio et al., 2018).

Altogether, they serve as the basis for understanding the emergence of FCD by changes in local circuits and subnetworks. However, a systematic exploration of the relationship between global structural connectivity and FCD has not been undertaken.

At mesoscale, coupling (Deco et al., 2009; Deco and Jirsa, 2012) and delay between nodes (Deco et al., 2009; Cabral et al., 2014) have been suggested as mechanisms that could drive the system to different states.

At the macroscale, the relationship between FCD and the network’s structure has remained elusive. While most of the studies aimed at establishing a causal link between a given structure and its associated functional connectivity dynamics (Batista-García-Ramó and Fernández-Verdecia, 2018; Honey et al., 2009), little attention has been paid to *how* does the network structure could drive the dynamics.

Additionally, FCD has been described to change in different contexts such as anesthesia (Hutchison et al., 2013), aging (Tian et al., 2018) or psychiatric disseases (Fornito and Harrison, 2012), suggesting that FCD may account for more complex processes, such as

learning, memory or adaptation to an ever-changing environment or even consciousness (Preti et al., 2017).

The structural connectivity (SC) represents the physical connections between brain areas (Sporns et al., 2005). These connections can be observed in living subjects by mapping through Diffusion Tensor Imaging based on Magnetic Resonance Imaging (DTI-MRI), which shows the axonic fiber bundles that link different anatomical areas (Fornito et al., 2015). As Sporns hypothesizes (Sporns et al., 2005), “the pattern of elements and connections as captured in the connectome places specific constraints on brain dynamics, and thus shapes the operations and processes of human cognition”. Several pieces of evidence have supported the latter hypothesis, by establishing links between SC and FC. For example, Honey showed that the spatial statistics of FC can be related to the SC(Honey et al., 2009). Also, it has been shown that there is a strong relationship between the subnetworks found in FC and structural subnetworks observed in SC(Diez et al., 2015; Honey et al., 2007).

Relationships between SC and FCD have also been found, emphasizing even more the constraints that structural connectivity imposes on brain dynamics. Clinical observations in psychiatric disorders show that disruptions in specific properties of SC are correlated with changes in FCD such as schizophrenia (Dong et al., 2018), Major Depressive Disorder (MDD) (Zhi et al., 2018), bipolar disorder (Nguyen et al., 2017), Borderline Personality Disorder (Xu et al., 2016) or Alzheimer Disease (Schumacher et al., 2019).

The interaction between SC and FCD may be explained by the topological properties that the connectome has. The fact that the SC can be thought of as a network, by depicting anatomical structures as nodes, and connections between those areas as edges, allowed further studies by using network theory(Bassett and Bullmore, 2006, 2017; Park and Friston, 2013). For example, network studies on SC of different species have revealed complex network properties (for a review see (Van den Heuvel et al., 2016)). In particular, studies on the human connectome have shown “ that brain anatomical connectivity is sparse, locally clustered, and with a few long-range connections mediating short path lengths between any pair of regions”, which is known as small-world topology (Bassett and Bullmore, 2006). This particular property, small-worldness,

is thought to account for different state transitions, which integrate and segregate information, driving cognition and behavior(Cohen and D'Esposito, 2016; Deco et al., 2015; Sporns, 2013).

Interestingly, experiments involving the extirpation of one hemisphere –hemispherectomy–, show that the small-world property of SC does not always correlate with FCD. For example, hemispherectomy in rats does not affect significantly the FCD (Otte et al., 2015), but it does changes the SC because interhemispheric connectivity has been removed. In humans, it has been shown that after a hemispherectomy, the language abilities in children are partially preserved (Ivanova et al., 2017). Also, some author reports that "patients with intact bilateral resting-state functional connectivity have been reported in the absence of major commissural fibers"(Uddin, 2013). Thus, is it a small world property necessary for inducing and supporting FCD? Could any other topology, besides the small world, support FCD? Is there any "optimal" network structure that maximizes states and dynamical richness in FCD?

To investigate the relationship between topological properties of the SC and the dynamical richness and state transitions in FCD, we implement a model of neural activity based on a modified version of Huber & Braun's model (HB+Ih) (Orio et al., 2012, 2018; Xu et al., 2018), connecting them in a network with different topologies, ranging from regular to random networks(Watts and Strogatz, 1998). We then studied FCD by measuring the pairwise envelope's correlation and by measuring "activity states."

Understanding the structural topological properties that drive a plethora of dynamic states in networks would be invaluable to broaden our understanding in the relationship of structural connectivity changes observed in psychiatric diseases, or understanding cognitive processes, such as learning and memory. Additionally, in a more abstract way, the knowledge of a specific network structure that increases the repertoire of responses given certain input would improve current algorithms in machine learning and artificial intelligence, enhancing technological advances.

Chapter 2

Hypothesis and Objectives

2.1 HYPOTHESIS

The small world property of Structural Connectivity shapes the dynamical richness observed in dynamical Functional Connectivity in a large-scale brain network model.

2.2 MAIN OBJECTIVE

Explore the relationship between network structure and network dynamics, by using a biophysically inspired neural oscillator in small-world networks.

2.3 SPECIFIC OBJECTIVES

1. Simulate global activity in different small world networks composed by modified Huber-Braun oscillator.
2. Measure multistability, metastability, number of states, and global synchrony of the simulated system.
3. Compare the relationship between small-world properties and dynamical properties measured previously.

Chapter 3

Methodology

3.1 NETWORKS

Network models were implemented, as they provide a more robust element on which experiments could be performed. For this, the Watts-Strogatz model was used.

For network characterization and comparison, metrics that describe the network's "capacity" to integrate or segregate its nodes were used. Additionally, metrics that quantify to what extent this integration or segregation is present, namely the small world, were also calculated.

3.1.1 Network Models

Artificial small world networks (SWN) were generated by Watts-Strogatz algorithm (Watts and Strogatz, 1998). Briefly, this algorithm starts with a latticed network, on which each node is connected with its closest $k/2$ left neighbours and its closest $k/2$ right neighbours. Then, by randomly rearranging the connections between nodes with probability p, one may transit from the latticed matrix ($p = 0{,}00$) to a completely random network ($p = 1{,}00$). For every pair of reconnection probability p ($p \in \{0{,}00; 0{,}01; 0{,}05; 0{,}10; 0{,}20; 1{,}00\}$ and node degree k ($k \in \{4, 10, 20\}$), four networks of 250 nodes were constructed.

3.1.2 Segregation and integration metrics

Segregation is the network's characteristic that expresses the ability for processing specialized information in a particular subset of the network. It is related to the number of clusters or modules within the network (Rubinov and Sporns, 2010). On the other hand, integration is the network's ability to put together all the information that is processed in different parts of it. It is

related to the path or sequence of steps that a node q needs to travel for arriving at another node r (Rubinov and Sporns, 2010). Calculation of the integration and segregation metrics were done by using the brain connectivity toolbox for Python, *bctp*[1]

3.1.2.1 Clustering coefficient

Clustering coefficient is a measure of segregation that reflects the probability that neighbors of a node are also connected, in other words, it counts how many triangles are in the network (Watts and Strogatz, 1998).

The clustering coefficient is calculated as

$$C = \frac{1}{N} \sum_{i}^{N} \frac{2n_i}{k_i(k_i - 1)}$$

Where N is the total number of edges, and n_i are the edges existing between neighbors of node i. k_i is the degree of node i.

3.1.2.2 Transitivity

Transitivity is a variant measurement of the clustering coefficient (Rubinov and Sporns, 2010). Transitivity, as being collectively normalized, does not suffer the low degree influences observed in clustering coefficient (Rubinov and Sporns, 2010).

Transitivity (τ) is defined as

$$\tau = \frac{\sum_{i \in N} 2t_i}{\sum_{i \in N} k_i(k_i - 1)}$$

Where t_i is the number of triangles

$$t_i = \sum_{j,h \in N} a_{ij} a_{jh} a_{ih}$$

and a_{xy} is the connection between nodes x, y

[1] https://pypi.org/project/bctpy/

3.1.2.3 Modularity (Q)

The network modularity is another measure of network segregation (Newman, 2004). Modularity Q is the difference between the number of edges that lie within a cluster in the studied network and a random equivalent network. This is done by computing Q with the function *modularity* from bctpy toolbox (Rubinov and Sporns, 2010).

$$Q = \frac{1}{m} \sum_{ij} \left[a_{ij} - \frac{k_i^{in} k_j^{out}}{m} \right] \delta_{c_i, c_j}$$

where:

- m: total number of edges of the network
- a_{ij}: element of the adjacency matrix. $0, 1$ in this work
- k_i^{in}: in degree of node i
- k_j^{out}: out degree of node j
- δ_{c_i, c_j}: Kronnecker's delta. One if nodes i, j belongs to the same module c

3.1.2.4 Characteristic path length

A path is defined as the number of nodes that one needs to travel from node x to arrive at node y. If two or more paths exist between nodes x, y, the shortest one is preferred. The characteristic path length is the average of the shortest path length of the whole network (Watts and Strogatz, 1998). This metric characterizes the integration of the network, as networks with short characteristic path length, l indicates that, for every node in the network, every other node is l nodes away. The characteristic path length for disconnected nodes is defined as infinite.

3.1.2.5 Efficiency

Characteristic path length tends to be influenced by longer paths. Efficiency, which is the inverse of the characteristic path length, tends to be influenced by shorter paths and it is preferred for characterizing integration (Rubinov and Sporns, 2010), as it also represents how the information is flowing across the network (Latora and Marchiori, 2001).

$$\eta = \frac{1}{N(N-1)} \sum_{x \neq y} \frac{1}{d_{xy}}$$

Where d_{xy} is the shortest distance between nodes x, y

3.1.3 Small World metrics

The small-world property has been established for large networks (1000 nodes or higher) (Humphries and Gurney, 2008; Muldoon et al., 2016; Neal, 2017; Telesford et al., 2011; Watts and Strogatz, 1998). Nevertheless, no systematic approach has been taken for defining the small-world property on small-sized networks. Additionally, no consensus exists on how to define a small-world network. Watts and Strogatz (Watts and Strogatz, 1998) defined that a small-world network is a network that is highly clusterized, resembling a regular network, but with short path length, as it is observed in random networks. However, no analysis has been done when the network size diminishes.

To account for the small world feature of the network and select the one that best represents this characteristic, four different metrics were computed: Humphries & Gurney's Small Worldness, σ (Humphries and Gurney, 2008); Telesford's Small-World metric, ω (Telesford et al., 2011), Muldoon's Small-World propensity, ϕ (Muldoon et al., 2016) and Neal's Small-Wold index, SWI (Neal, 2017). In particular, the calculation of these metrics involves the comparison with a null model of the equivalent random or latticed network. For that purpose, regular or random equivalent matrices were created by using the Watts-Strogatz algorithm, with a reconnection probability of 0 or 1, accordingly.

3.1.3.1 Small-Worldness index σ

This metric tests if any given matrix has small-world topology or not (Humphries and Gurney, 2008). To do this, the properties of the analyzed network, X_m, are contrasted with the same properties of a random one, X_{rand}. For this, the minimum number of edges that must be traversed to get from one node to the other or characteristic *minimum path-length*, L_m, and the *clustering coefficient*, C_m, were calculated. Then, the small-worldness index is calculated as

$$\sigma = \frac{\gamma}{\lambda}$$

Where

$$\gamma = \frac{C_m}{C_{rand}}$$

and

$$\lambda = \frac{L_m}{L_{rand}}$$

Thus, a network is said to have small world properties if $\sigma > 1$.

3.1.3.2 Small World index ω

Because the Humphries index offers a binary classification for a given network, small-world ($\sigma > 1$) or not ($\sigma \leq 1$), it is not useful for assessing *how* much small-world it is. For that reason, Telesford proposed a new index that allows classifying a network in small-world, regular, random, and in between (Telesford et al., 2011). If $\omega = 0$, the network is considered a small-world. On the other hand, if $\omega = 1$, it is said to be a regular network, and for $\omega = -1$, the network is random. Thus a network could be "more" small world if $\omega \approx 0$. The new metric proposed, $\omega \in [-1, 1]$, is defined as

$$\omega = \frac{L_{rand}}{L_m} - \frac{C_m}{C_{lat}}$$

where C_{lat} is an equivalent latticed network. Notice that the clustering coefficient C is normalized with respect to a lattice equivalent network, and not to a random one (Telesford et al., 2011).

3.1.3.3 Small World propensity ϕ

One of the critiques proposed to the previous metrics is that they are density-dependent (Muldoon et al., 2016). To convey that issue, Muldoon and collaborators proposed a new metric for assessing the smallworldlness of a network, regardless of its density. When the network's density is increased, the clustering coefficient and path length diminish. Small world propensity ϕ quantifies if a network describes small-world property and accounts for changes in density.

$$\phi = 1 - \sqrt{\frac{\Delta_c^2 + \Delta_L^2}{2}}$$

where

$$\Delta_c = \frac{C_{latt} - C_{obs}}{C_{latt} - C_{rand}}$$

and

$$\Delta_L = \frac{L_{obs} - L_{rand}}{L_{latt} - L_{rand}}$$

C_{obs}, L_{obs} correspond to the clustering coefficient or path length of the observed network, respectively. $(C, L)_{latt}; (C, L)_{rand}$ corresponds to the clustering coefficient or path length of the null model of the random or latticed network.

Networks with high small-world characteristics will have a ϕ value closer to 1. Lower values of ϕ represent a less small-world structure (Muldoon et al., 2016).

3.1.3.4 Small World Index (SWI)

Critiques to the ω metric proposed by Telesford (Telesford et al., 2011) reveal that if the difference between the clustering coefficient or mean path length in random and latticed networks is small, ω gives false positives on the criteria for assessing the small-world property (Neal, 2017). Additionally, it is proposed that ω analyzes whether the network matches a clustering coefficient similar to a latticed network *or* a path length similar to a random one (Neal, 2017). To solve this, a new metric should check if both small world conditions are met, i.e., clustering

coefficient must be similar to latticed network *and* path length similar to a random one (Neal, 2017).

For doing that, Neal proposed the metric SWI (which will be refered as ξ in this work) as

$$\xi = \frac{(L - L_l)}{(L_r - L_l)} \frac{(C - C_r)}{(C_l - C_r)}$$

Where L, C corresponds to path length and clustering coefficient, and l, r represents the equivalent latticed or random network(Neal, 2017).

3.2 SIMULATION

3.2.1 Node dynamics

For modeling node activity, a modified Huber & Braun (HB) neural model was used. This particular model (namely, HB+Ih) contains an additional hyperpolarization-activated current, I_h, that allows the model to exhibit regular or chaotic oscillations if the relationship of conductances is changed while preserving its firing properties (Orio et al., 2018). The full model can be found in the Supplementary Information (Appendix A).

HB+Ih nodes were connected using SWN as adjacency matrix (see 3.1.1) . Two neurons j, k are connected by an electrical coupling g, if the element in the adjacency matrix $C_{jk} = 1$. In other words

$$I_k^{gap} = \sum_{j=1, j \neq k}^{N} C_{jk} g(V_j - V_k) \tag{3.1}$$

3.2.2 Heterogeneous nodes

For simulating diversity in the network, for every node, its parameters g_{sr}, g_{sd} were chosen randomly from a set of 194 values that granted either chaotic or non-chaotic behavior, maintaining

its firing rate between 3.0 - 4.5 spikes/s. Even though both sets of parameters, chaotic and non-chaotic, were employed, only chaotic behavior was analyzed in this work.

3.2.3 Initial conditions

For each node, initial voltage $V_k(0)$ was selected randomly from an uniform distribution $U(a, b)$, where $a = -70, b = -50$. Temperature was fixed at 36°C and $a_d(0), a_r(0), a_{sd}(0), a_h(0)$ were calculated accordingly to these initial voltages.

3.2.4 Dynamical simulation

Eighteen values of the network's nodes coupling g between $\{0\} \cup [0{,}0001, 1]$, were selected[2] For every value of g, transient was simulated for 30 s ($dt = 0{,}05ms$) without noise for system stabilization, and then for 202 s ($dt = 0{,}05ms$) with a fixed multiplicative noise value to obtain the system's dynamical behavior. In this model, the noise is inversely proportional to the cell's membrane area, thus several area values were used (500, 5 x 10^4, 5 x 10^5, 10^{12}). For solving the system, the Euler method was used for the transient calculation, while the Maruyama-Euler method was used for calculations under noise conditions (Laing and Lord, 2010). The details of the calculation, as well as the model used for the simulation are shown in the Supplementary Information (Appendix A).

3.2.5 Signal preprocessing

Every simulated time series was subsampled at 4 kHz, filtered with a low-pass filter for obtaining the subthreshold oscillation (Bessel 4th order, ω_{cut} =50Hz). After that, the signal was downsampled to 200 Hz and filtered again with a band-pass filter (Bessel, 4th order, $\omega_{cut} = max\{\omega_i\} \pm$ 3 Hz, where w_i is the mean frequency of HB oscillator). Hilbert transform was then

[2] the set is defined as $g = \{0\} \cup \{x \in \mathbb{R} : \mathrm{x} = 10^{(-4+4*\mathrm{k}/16)}, \mathrm{k} \in \mathbb{N} : \mathrm{k} = \{0 \dots 16\}\}$

applied for obtaining the instantaneous phase of the slow oscillation. The first and the last second of the simulation were discarded to get rid of the artifacts that Hilbert transform may generate. This signal was used for assessing dynamical analysis.

3.3 ANALYSIS

3.3.1 Synchrony measures

Kuramoto order parameter $R(t)$ was calculated for every simulation as

$$R(t) = \frac{1}{N}|\sum_{k=1}^{N} e^{i\phi_k(t)}| \tag{3.2}$$

Where i is the complex unit and $\phi_k(t)$ is the instantaneous phase of the k-th node. Then, **Global synchrony** was calculated as the time average of $R(t)$ and **Metastability,** χ**,** was calculated as the variance of $R(t)$

$$\chi = \frac{1}{n}\sum^{n}(\langle R\rangle_T - R)^2 \tag{3.3}$$

Where n is the number of points that the signal R has, and $\langle R\rangle_T$ is the average in time of the global synchrony.

3.3.2 Functional Connectivity (FC)

The statistical dependency of neural signals was measured through a Functional Connectivity (FC) matrix (Messé et al., 2015). Every element of this matrix corresponds to the pairwise phase synchrony between nodes j, k, averaged over a time window of duration W.

$$FC_{j,k} = R_{j,k} = \left\langle \left| \frac{1}{2}(e^{i\phi_j(t)} + e^{i\phi_k(t)}) \right| \right\rangle_W \tag{3.4}$$

3.3.3 Functional Connectivity Dynamics (FCD)

The concurrency of FC patterns is captured through a Functional Connectivity Dynamics (FCD) matrix, which displays the dynamical repertoire of the system. To calculate the FCD, windowed FCs matrices were calculated(time windows of 2 s, overlap = 75 %). Then, the Clarkson Distance between the vectorized lower triangular of FC_i and FC_j was calculated.

$$FCD_{i,j} = \left|\left| \frac{FC_i}{||FC_i||} - \frac{FC_j}{||FC_j||} \right|\right| \tag{3.5}$$

3.3.4 FCD clustering

As reported previously, in order to find long-lasting or repeating patterns of correlations, namely states, in the dynamics of the system, we used an unsupervised clustering analysis (Orio et al., 2018). Briefly, we performed a Principal Component Analysis (PCA) on a matrix containing the FCs in their vector form. Then, we computed the Euclidean distance between all FCs projected on the first five principal components. In this space, we used an adapted version (Yger et al., 2018) of the Density-based Clustering (Rodriguez and Laio, 2014) to automatically find the centroids of the clusters.

Chapter 4

Results

4.1 NETWORK SMALL-WORLDNESS IS SHAPED BY NETWORK DENSITY, NODE NUMBERS, AND RECONNECTION PROBABILITY

In order to select the number of nodes that will be used in the network, several Watts-Strogatz networks with different node number (9 values), reconnection probability (18 values), and density (5 or 7 values, according to the network size) were built. For each parameter combination of node number, density and reconnection probability, 10 realizations of the network were constructed and the previously proposed small-world metrics (σ, ω, ϕ, SWI) were calculated and averaged, to assess which metric best represents the small-world property of the network.

In figure 4.1, a summary of the small world measurements is shown, as the node number (columns), reconnection probability (in x-axis), and network density (colors) are increased. Note that in the 20 node configuration, densities lower than 0.1 are not used as they impose a topology that allows nodes to be disconnected. Reconnection probability between 0.05 and 0.15 generates networks with small-world properties for networks over 250 nodes.

Interestingly, for all networks, $\sigma > 1$. This indicates a small-world property (Humphries and Gurney, 2008), even when the created network was regular ($p = 0{,}00$).

In the case of ω, values closer to 0 are indicative of small world networks (Telesford et al., 2011). This behavior is best observed in networks with $\delta < 0{,}25$ and with more than 50 nodes (4.1 ω with 250 and 2000 nodes and in figures C.1 and C.2). It can be observed that this metric is the only one that can differentiate between regular ($p = 0{,}00$) and random ($p = 1{,}00$) networks.

In the ϕ and χ metrics, values close to 1 suggest a small-world network. Both metrics exhibit a maximum with a reconnection probability similar to the one observed where $\omega \approx 0$. However, it is not possible to discriminate between regular or random networks.

The metric ω allows differentiation between regular, small world, and random

networks, as it provides a continuum between those three topologies. For the rest of this work, networks that have $\omega \in [-0{,}25, 0{,}25]$ will be considered small-world. This is a narrower range than the one used by Telesford (Telesford et al., 2011). The selected range of ω implies that networks with reconnection probability $p \in [0{,}05, 0{,}30]$ are small-world. Finally, densities $\delta \leq 0{,}2$ will be used as they span the higher range of separability between the regular, small world and random topology.

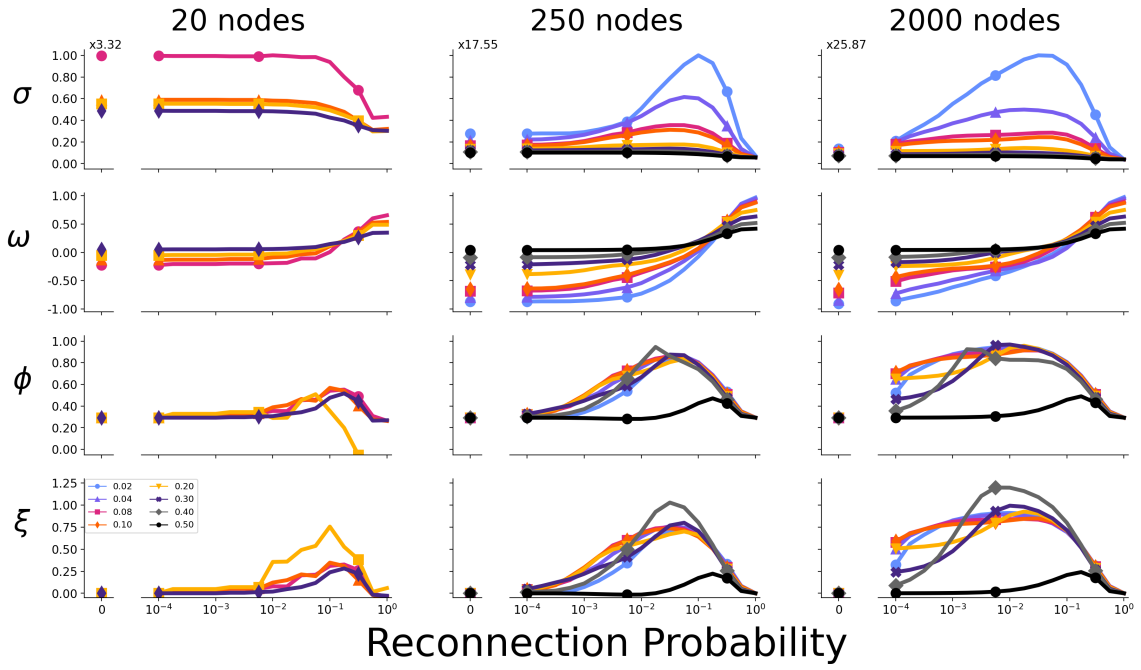

FIGURE 4.1: **Network Small-worldIness metrics**. Different node numbers, density, or reconnection probability were used for calculating small-world metrics. Notice that in σ, plots were scaled for visualization purposes. Full node ranges are available in supplementary figures

4.2 SIMULATION, DATA GENERATION AND ANALYSIS

Networks with 250 nodes and different densities ($\delta = 0{,}02; 0{,}04; 0{,}08$) were created for studying the dynamics under different topologies (figure 4.2 A). Networks are composed of heterogeneous nodes, as parameters g_{sr}, g_{sd} were randomly chosen such as each node would have chaotic behavior with a firing rate between 3.0 and 4.5 spikes/s (Orio et al., 2018; Xu et al., 2018). Then, the coupling strength between the nodes was increased in logarithmic steps from 0 to 1. Additionally, multiplicative noise was incorporated into each node, to resemble the stochastic

opening of ion channels (Orio et al., 2012). Simulated signals were filtered, downsampled and a Hilbert Transform was used to obtain the analytic signal's phase of the slow oscillation (figure 4.2 B). Functional Connectivity (FC) (figure 4.2 C) was calculated for different time windows(window size = 400 points, equivalent to 5 ms; overlap = $75\,\%$), by calculating the pairwise phase synchrony between the phase of each signal (250 in total). Functional Connectivity Dynamics (FCD) was then calculated by computing the pairwise Clarkson distance between FCs (figure 4.2 D). Finally, density-based clustering was conducted in FCs in order to calculate state numbers (see Methods).

The FCD matrix shown in figure 4.2 D represents how different are the FCs through which the network transits. Therefore, the FCD is a representation of the network dynamics. When the coupling between nodes is $g = 0$ (figure 4.2 E), the FCD appears as constant green, meaning that the difference between FCs is constant but different from 0. In other words, the synchrony pattern evolves constantly without settling. This constant behavior is also observed in the histogram below it. It may be observed that the variance is zero, as there is only one value in the distribution of the FCD, outside the main diagonal.

Increasing the coupling causes the appearance of yellow and red patches in the FCD, meaning a greater and broader range of differences between FCs. This also is observed in the histograms, as the values present in FCD deviate from the constant value observed in $g = 0{,}0$ towards a distribution with higher variance. Also small values (blue) are observed, indicative of recurring synchronization patterns that have high similarity.

Finally, when coupling $g = 1{,}0$, the FCD matrix appears blue, meaning that the difference between FCs is zero and the synchronization pattern is only one static configuration. Inspecting the histogram of FCD under this condition show a single value distribution, leading to a variance equal to zero.

Taking all together, FCD provides a tool for measuring the dynamics of the network, while its variance provides a numeric value for relating this dynamic. The next sections will explore how the dynamical richness of the network captured by the FCD is related to the network's structural parameters.

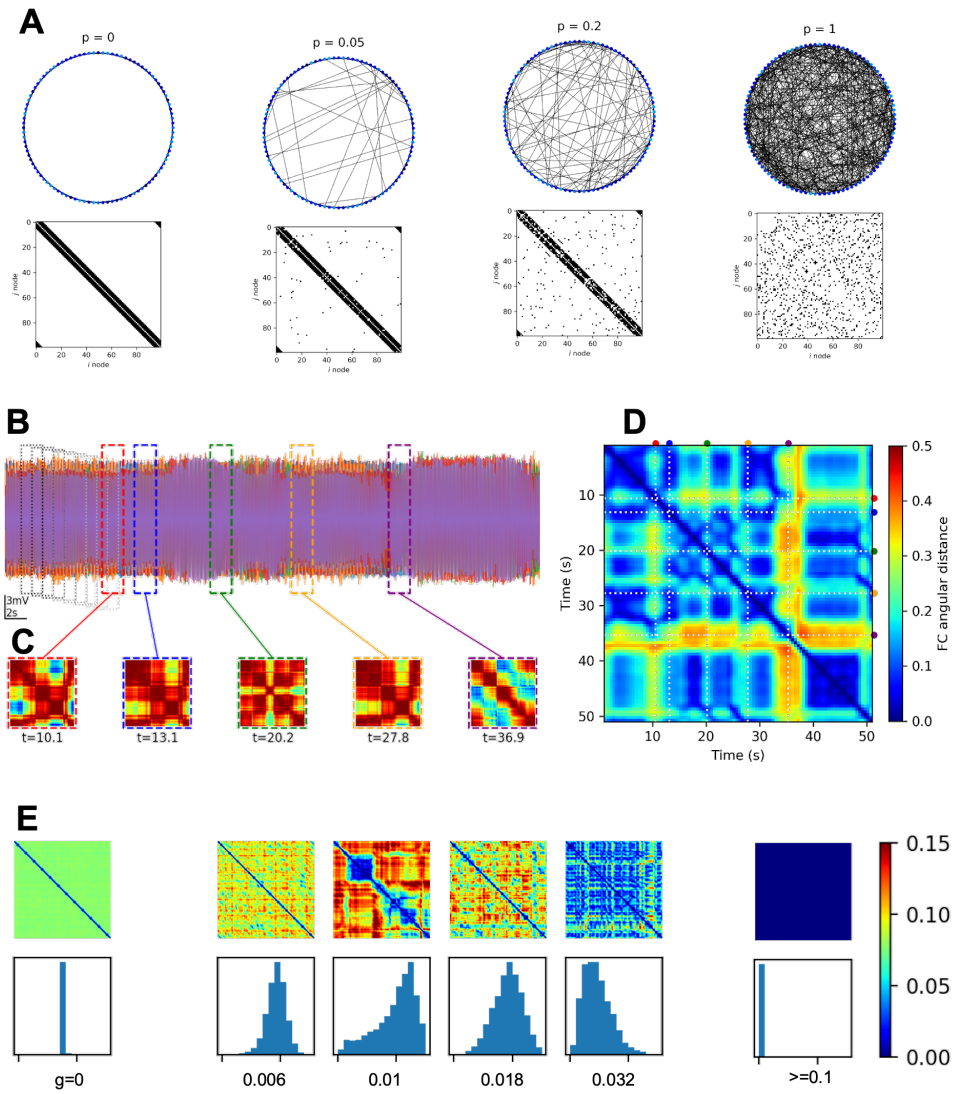

FIGURE 4.2: **Simulation Workflow**. In **A**, 100 node networks with same density but different reconnection probability were build. **B** Five trace signals of simulated nodes are shown. **C** As the time window is shifted, different Functional Connectivity (FC) networks are obtained using the [synchrony—phase locking] between the phase of the signals. **D** To represent the network dynamics, Functional Connectivity Dynamics is built by calculating the distance between vectorized FCs. Colored dots at the top of the FCD correspond to different FCs shown in B. **E** FCD dynamical richness is quantified by measuring its variance. Note that $Var(FCD_{g=0,00 \vee g \geq 0,1} = 0$, however in intermediate values of g $Var(FCD) \neq 0$. Panels B-E adapted from (Orio et al., 2018)

4.3 NETWORK TOPOLOGY DRIVES NETWORK DYNAMICS

FCDs generated by simulations with different coupling strength ($g \in [0{,}01; 1]$) and noise levels are plotted in Figure 4.3 (top). Additionally, the variance of FCD (bottom) was calculated and plotted, as it serves as a proxy for metastability (see Methods). Three characteristic networks with density $\delta = 4\,\%$ are shown ((Regular network ($p = 0{,}00$), small-world Network($p = 0{,}10$), and random network ($p = 1{,}00$)). Here, the value 500 is the maximum amount of noise, as it is related to the number of channels present in a fixed area. Increasing the area while maintaining channel density decreases the noise (Orio et al., 2018). Following that idea, a noise value of 10^{12} is a close approximation to the deterministic (noiseless) case.

As the connection strength is augmented in absence of noise in the regular network, $p = 0{,}00$ (4.3 Upper left. First row), it can be observed that FCD transits from a regular green color ($g = 0{,}01$), to a more diverse pattern of colors before reaching blue, static FC ($g = 1{,}00$). If the noise is increased without changing the coupling (4.3 Upper left, first column), the FCD transits from a regular pattern of activity (green) to another one (blue). On intermediate values of coupling and noise, it may be observed that the FCD exhibits patterns of colors, establishing a range with high dynamic activity (see also 4.2 E). The quantification of var(FCD) summarizes the previous results (bottom plot). It can be observed that the maximum value of var(FCD) is obtained for the deterministic condition (black trace, $1e + 12$) at coupling strength $g = 0{,}10$, which coincides with the reddish pattern observed in the FCD plots.

If the network is random, $p = 1{,}00$, when the connection strength is increased in the absence of noise (4.3 Upper right, first row), the FCD transits from green to blue, without the colored patterns observed in the regular network. Increasing the noise, without changing the coupling strength (4.3 Upper right, first column), the same pattern of activity observed in the FCD of the regular network is maintained. However, at intermediate values of coupling and noise, the colored patterns are lost, suggesting that random networks transit from one fixed state (green FCD) to another one (blue FCD), without a high dynamic activity, as observed in regular networks.

Finally, it may be observed that the dynamical richness, characterized by the variance

of FCD is reduced as the reconnection probability is increased. This is better characterized in the bottom plots. Var(FCD) is higher in the regular network(bottom left) and decreases in the small-world network (bottom middle) to almost disappear in random networks (bottom right).

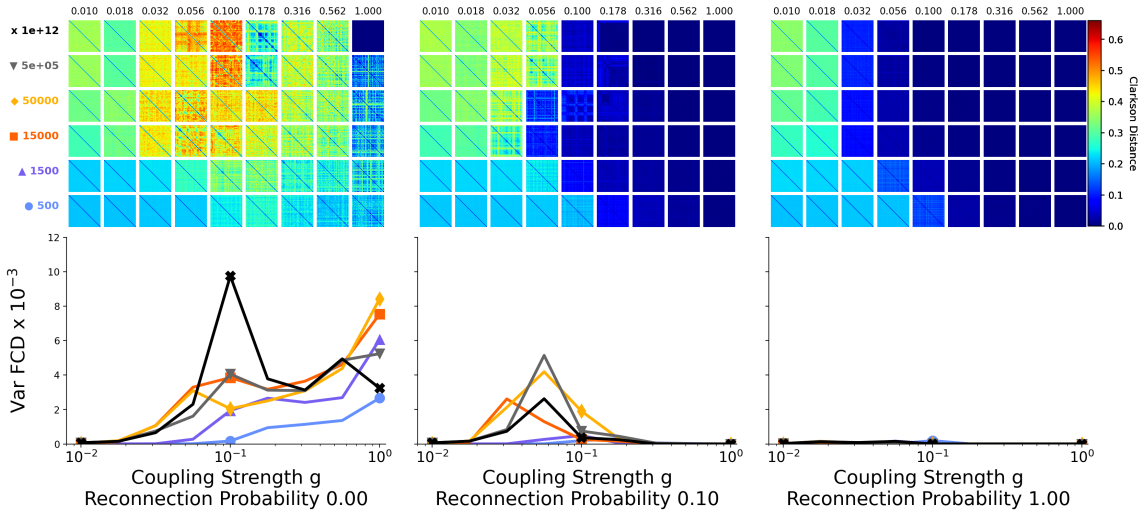

FIGURE 4.3: **Changes in FCD due to noise, connectivity strength and connection density.** The FCD patterns (top) of regular ($p = 0{,}00$, left), small world ($p = 0{,}10$, middle) and random ($p = 1{,}00$, right) are shown. The orange-red colors in the middle range of connection strength in a regular network represent a greater dynamic in the FCD and are disrupted if a random network is used (right). The variance of FCD is shown in the bottom plots. The X-axis represents coupling strength while the y-axis is the mean variance of FCD over 4 network realizations. Notice that low noise values, deterministic and $5e+05$, black and grey trace, respectively, yield the higher variance of FCD.

To better examinate this dynamical variations due to the structural connectivity observed in 4.3, Synchrony, Metastability (χ) and FCD variance were also analized. Synchrony, measures the phase synchrony of all the signals of the network, ranging from no synchronization (0), to fully synchronized (1); Metastability (ξ), measures the variability in time of the global synchrony; Variance of FCD is used as quantification for the dynamical diversity of the system. Note that while Metastability measures the time variation of global synchrony across all nodes in the network, the FCD analysis is based on the time-varying patterns of pair-wise synchronization. For a detailed explanation on the calculation of each metric, see Methods.

In figure 4.4, network's dynamical parameters behavior for noise=15000 are shown. Each column shows a particular density, and row shows one of the three dynamical parameters measured. Colors in each main plot represent reconnection probability. Insets show how noise changes the network's dynamical parameters behavior with a fixed reconnection probability of

$p = 0{,}10$.

It may be observed that networks with reconnection probability $p \geq 0{,}10$ achieve maximum synchrony, regardless of network's density, while networks with lower p do not fully synchronize. Additionally, highly synchronized networks exhibit lower metastability and FCD variance than the no synchronized ones ($p = 0{,}00, p = 0{,}05$). Noise intensity affects the network's dynamic regime in different ways. Higher noise makes the network less easy to synchronize(insets in top row, red line) but enhances metastability(insets, middle row). On the contrary, lower and medium noise levels (inset, green and black lines) enhance var(FCD) in networks, regardless of their density. Finally, cluster numbers tend to follow the var FCD, i.e., higher clusters are found in networks with high var FCD (not shown).

To summarize, noise and network density modulate the network's activity but they do not change the overall observed behavior, i.e., the network's activity decreases with the reconnection probability and the network's noise/density exerts their effect within the dynamical range imposed by the reconnection probability. This is consistent with previous works (Orio et al., 2018; Xu et al., 2018).

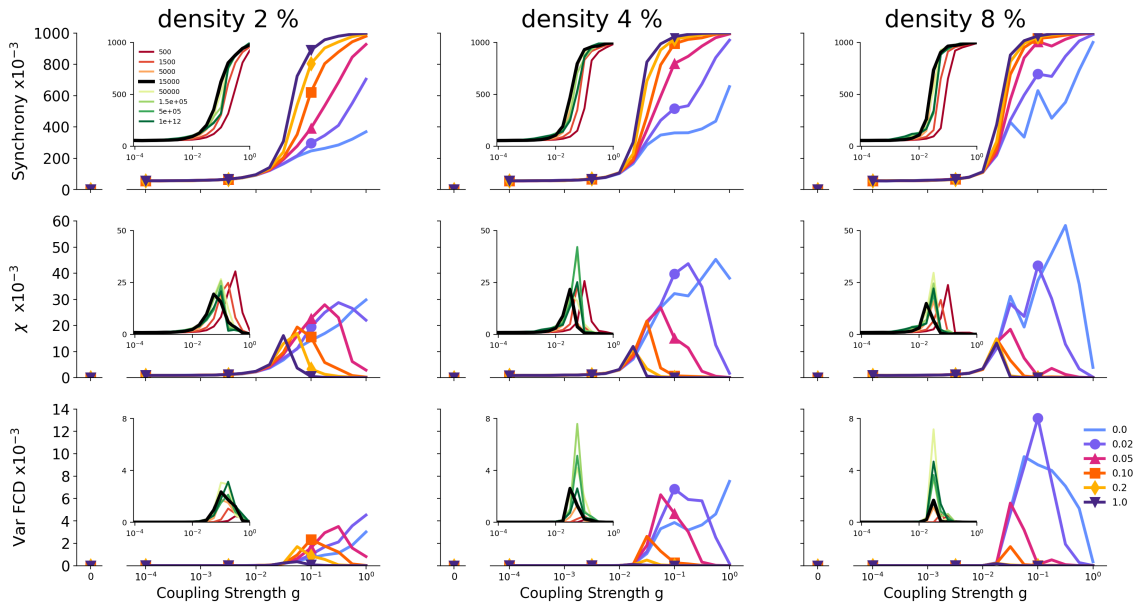

FIGURE 4.4: **Dynamical parameters change with reconnection probability**. Network's behavior of three dynamical metrics(rows), for three different densities(columns) and noise=15000 as the coupling parameter is increased, are shown. Colors represent different reconnection probabilities ranging from regular network ($p = 0{,}00$) to random ($p = 1{,}00$). Insets show how the noise changes the dynamical parameter of the main plot, as the reconnection probability is fixed ($p = 0{,}10$). Inset line colors range from green(low noise) to red (high noise). The black line corresponds to the noise level of the main plot (15000). All values correspond to mean values over four realizations.

4.4 NETWORK SMALL WORLD METRIC ω IS INVERSELY CORRELATED WITH NETWORK DYNAMIC

To establish a relation between structure and dynamics in the network, structural metrics related to network segregation(transitivity, network's modularity Q), network integration (efficiency), and the balance between segregation and integration, namely small-worldliness (ω), were contrasted against two dynamical parameters that relate the existence of multiple coexisting attractors or states (Multistability) (Friston, 1997), and the transitions between those states (FCD variance) (Kelso, 2012).

For each network, and for each noise level, the measures of metastability and varFCD along the connection strength axis were summarized into a single number by calculating the area under the curve (AUC). This area was then plotted against the structural parameters, as it is shown

in figure 4.5.

Inspection of the structure-dynamic plots suggests an exponential-like relationship between the analyzed parameters. In particular, it is observed that var(FCD) and metastability are inversely proportional to efficiency (η) and $omega$, but are directly proportional to transitivity (τ) and Q. In other words, var(FCD) and metastability are directly related to an increase in the segregation of the network and are inversely related to network integration.

To quantify these relationships, structural(x) and dynamical (y) observations were fitted into an exponential model, for every noise level. The fit was made using a linear regression to the expression $\log y_i = \log a + b * x_i$[1].

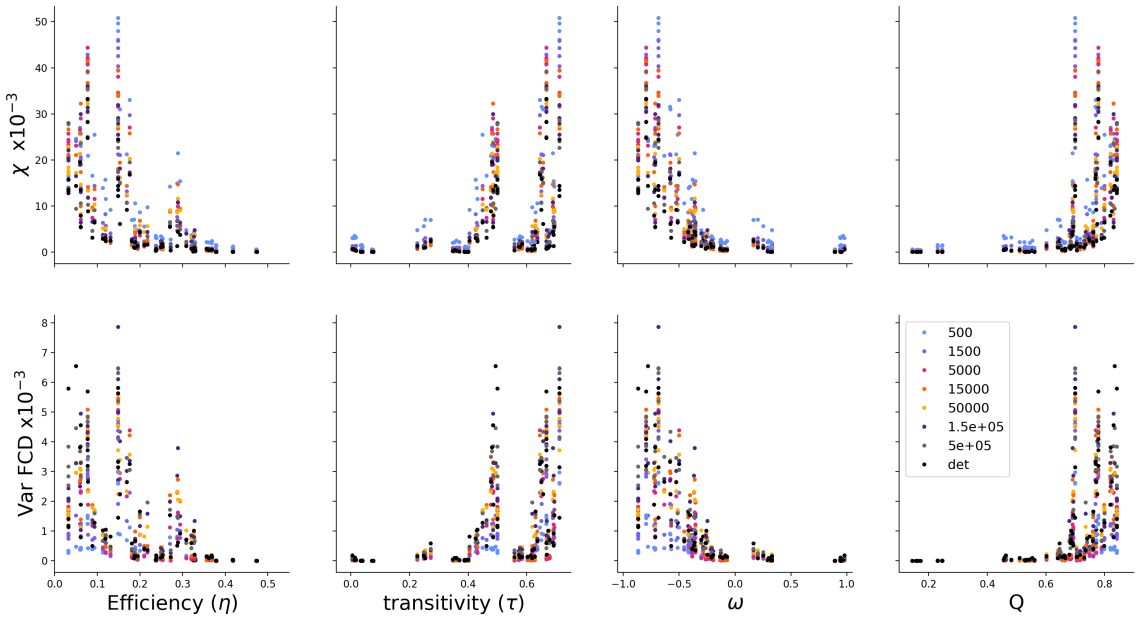

FIGURE 4.5: **Relationship between structural (efficiency, transitivity) and dynamical properties of the network.** Each point corresponds to the AUC, and the color represents the noise level for that particular point. All densities are represented in these plots.

Figures 4.6 and 4.7 show the best fit for metastability (χ) or var(FCD) with the four structural parameters. For sake of visualization, three levels of noise, averaged over four realizations, are shown.

[1] `https://docs.scipy.org/doc/scipy/reference/generated/scipy.stats.linregress.html`

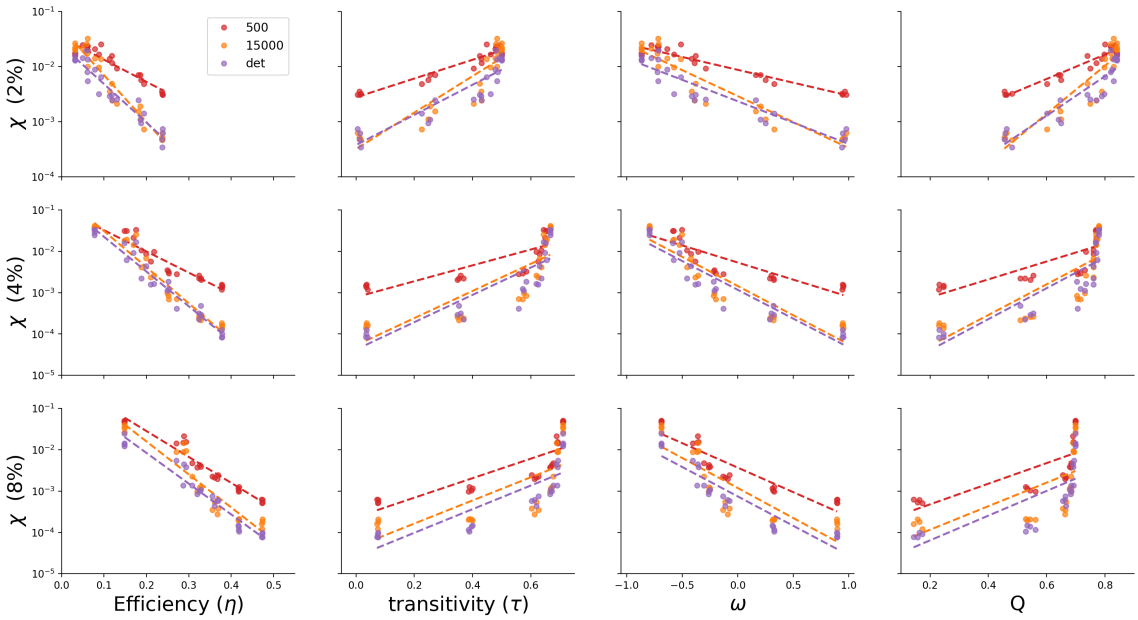

FIGURE 4.6: **Linearized structural-dynamical relationship for Metastability.** High (500), medium (15000, same as figure 4.4), and zero(deterministic) noise levels are shown.

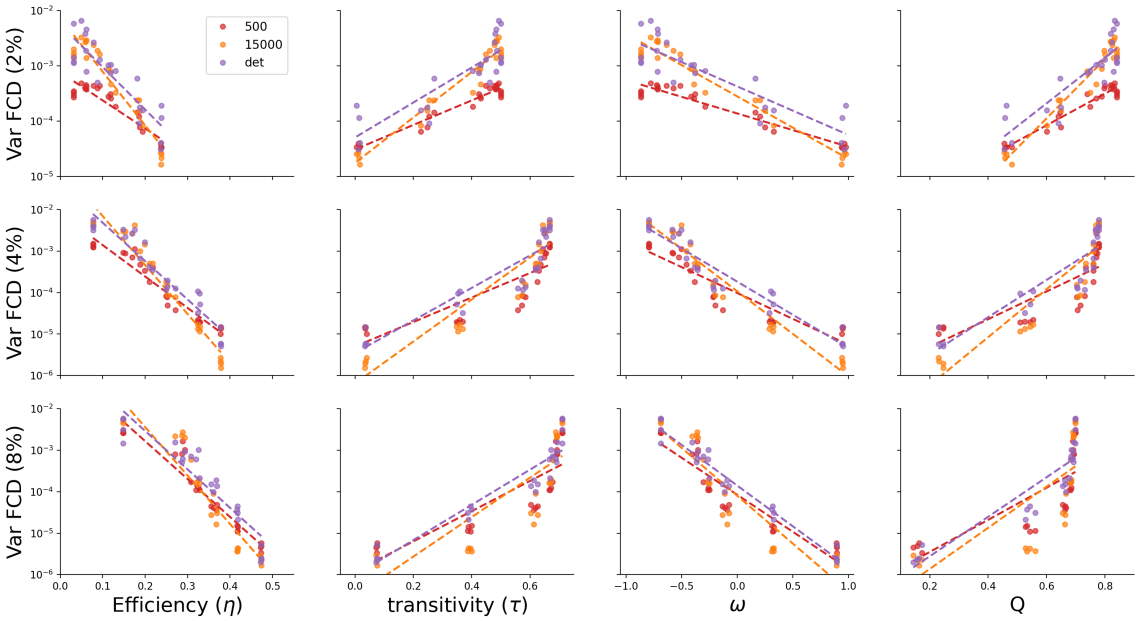

FIGURE 4.7: **Linealized structural-dynamical relationship for var(FCD). High (500), medium (15000, same as figure 4.4), and zero(deterministic) noise levels are shown.**

Finally, to evaluate which structural variables explain better the dynamical variables, root mean square error ($RMSE$), and correlation coefficient (R^2) was calculated for every noise level, and for densities of 2,4 and 8 %. Figure 4.8 and 4.9 show the $RMSE$ and R^2 for each

noise level, for metastability and var(FCD), respectively. For every density, metastability is best explained by efficiency (figure 4.8 middle and right columns). Although ω has lower $RMSE$ for some intermediate noise levels, the difference between that value and the $RMSE$ obtained by efficiency is small. Moreover, R^2 is higher for efficiency, regardless of noise level. Thus, efficiency (η) is, overall, the variable that best correlates with χ.

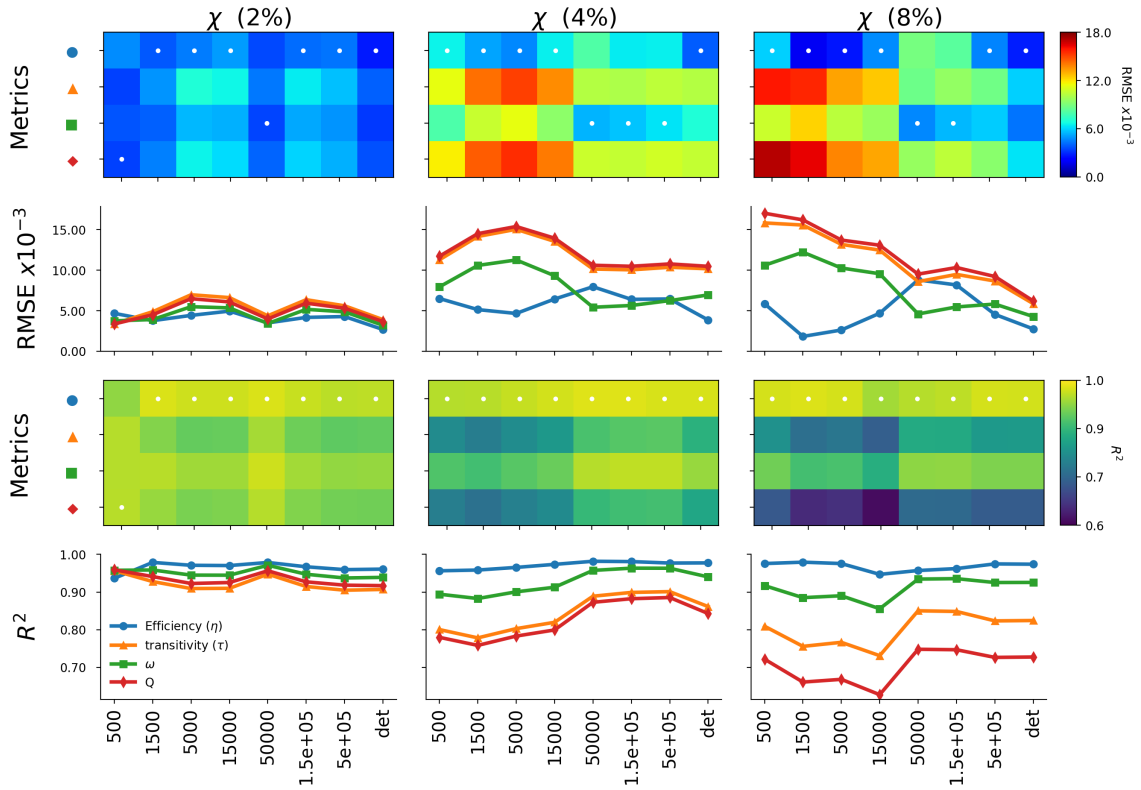

FIGURE 4.8: **Correlation analysis between Metastability and structural parameters.** Rows show the heatmaps and line plot for $RMSE$ (top plots) and R^2 (bottom plots) for the linealized relationship shown previously (fig. (4.6). Columns represent the networks with different densities. White dot on the heatmaps represents the minimum ($RMSE$) and the maximum (R^2) values observed for each noise level.

When the relationship for the variance of FCD is analyzed at $\delta = 2\,\%$(4.9 left column), it is not possible to establish which metric the best correlated variable for var(FCD), because $RMSE$ and R^2 are extremely similar for each of structural variables, regardless of noise levels. At 4 % and 8 % density, ω $RMSE$ is the lowest, even though R^2 is slightly higher for efficiency. However, as ω and efficiency show the higher R^2, the $RMSE$ of efficiency is the highest, and thus, it is possible to consider ω as the variable that best correlates with Var(FCD).

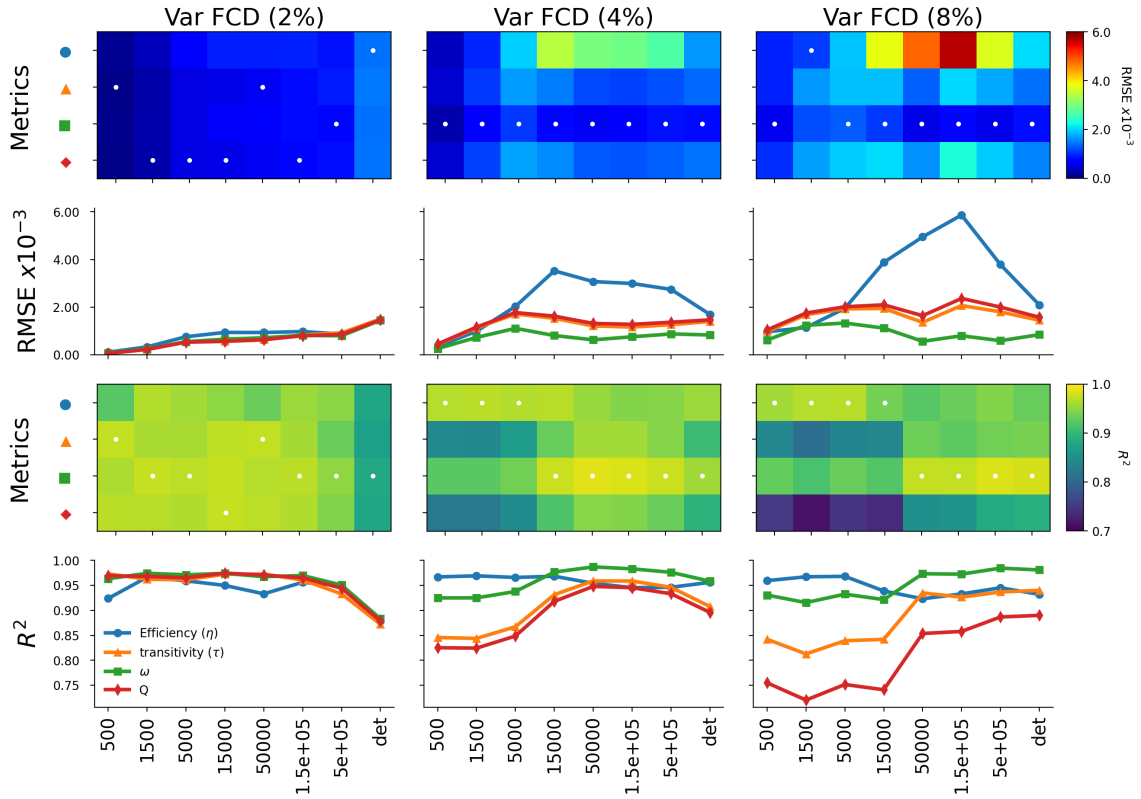

FIGURE 4.9: **Correlation analysis between Var(FCD) and structural parameters.** Rows show the heatmaps and line plot for $RMSE$ (top plots) and R^2 (bottom plots) for the linearized relationship shown previously (fig. (4.7). Columns represent the networks with different densities. The white dot on the heatmaps represents the minimum ($RMSE$) and the maximum (R^2) values observed for each noise level.

To summarize, Metastability χ is best explained by an inverse correlation with efficiency η, and Var(FCD), a proxy for multistability, is best explained by an inverse correlation with small world metric ω

$$\chi \quad \propto^{-1} \quad \eta$$

$$Var(FCD) \quad \propto^{-1} \quad \omega$$

Chapter 5

Discussion

In this work, I explored the relationship between network structure and function, by focusing on the interaction between regular, small world, or random network structure, and network dynamics characterized by multistability and metastability. It was observed that the network's dynamical richness is decreased as the reconnection probability is increased. Noise or density had only a modulatory effect on the dynamics within the range imposed by the structure of the network.

5.1 STRUCTURAL ANALYSIS OF NETWORKS

Analysis of the network's structural metrics such as global efficiency (η), Transitivity (τ) or Modularity(Q), under different node numbers, reconnection probabilities, and network's density, revealed consistency among node number or reconnection probability (Rubinov and Sporns, 2010). However, increasing network density had a homogenization effect, as the metric under study tended to be constant in the whole range of reconnection probability (fig. C.3). This is coherent with the relationship between the clustering coefficient and path length showed previously (Muldoon et al. (2016), supp. material). Higher densities mean high connectivity in the network, which could be thought of as a network behaving as a whole, which in turn increases integration. Thus, higher density implies higher efficiency.

Lower density values segregate the network, as it is more difficult to access from one node to another. Under this consideration, segregation should be high with low-density values and vice-versa. This is observed in the modularity metric Q, where lower density values mean high modularity. Transitivity, however, shows different behavior and could be a result of the definition of the calculation. Transitivity is a variant of the clustering coefficient, which counts how many triangles exist in the network. If the network is dense, there is a better chance to find more

triangles and hence clustering coefficient could be higher. Overall, these results are consistent with previous work that shows how node number, reconnection probability, and mean degree modifies the clustering coefficient and path length(Humphries and Gurney, 2008; Neal, 2017; Telesford et al., 2011; Van Wijk et al., 2010) (see also supp. figure C.1 and C.2)

Structural analysis of small-world networks revealed that irrespective of node number, the σ metric does not provide any information, as it considers every network as a small-world, regardless of node number, density, or reconnection probability, consistent with previous works (Muldoon et al., 2016; Neal, 2017; Telesford et al., 2011). On the other hand, simulations performed to analyze Small-world Propensity ϕ (Muldoon et al., 2016), and small-world index SWI (χ) (Neal, 2017), showed that these metrics are useful for assessing the degree of a network to exhibit small-world properties, regardless of its density(Muldoon et al., 2016) or network's size. As these metrics only relate to which extent a network approaches the "ideal" small-world network, they are not good for comparison among networks. The metric proposed by Telesford was tested not only for high node number as reported by the author (Telesford et al., 2011) but also for lower network's size (20 to 90 nodes). Telesford proposes that networks within the range $|\omega| < 0{,}50$ could be considered as a small-world network. With this in mind, the density shapes the range of ω, as networks with densities over 20 % are within this range, even if they are strictly regular ($p = 0$) or random ($p = 1$) (see also supp. figure C.1 and C.2).

A small-world network may be assumed if the network under study could be represented by a Watts-Strogatz network on which its reconnection probability lies within a certain interval. However, the selection of the interval is arbitrary and it is based on qualitative properties of the network and not on well-defined quantitative characteristics (Kaiser, 2011; Muldoon et al., 2016; Neal, 2017; Telesford et al., 2011; Watts and Strogatz, 1998).

The previous metrics has been tested on networks with fixed node number and different densities, or different node number ($n \geq 100$) and fixed densities. This drives the question on how many nodes should be used and how its "smallworldlness" can be characterized for a network with less than 100 nodes, how these metrics will behave on those networks, and ultimately, how accurate a network could model the human brain small-world structure (Bassett and Bullmore,

2006). In this work, it was shown that networks under 100 nodes could not be considered as small-world networks. The rationale behind this lies in the observation of the small world metric $omega$ (Neal, 2017; Telesford et al., 2011). In networks under 100 nodes, regular networks are depicted as "slightly non-regular"($\omega \geq -0{,}7$), but random networks are well classified. For networks with 250 nodes or higher, ω metric better represents the network's characteristic(fig. 4.1 and supp. figures C.1 and C.2).

Structural Connectomes derived from real data are constructed by dividing the brain into several anatomical regions. However, no consensus exists on how many areas should be used (Arslan et al., 2018). Because different connectomes parcels the brain in less than 100 nodes (Hagmann = 66 nodes (Hagmann et al., 2008); Budapest Connectome = 83 nodes (or higher) (Szalkai et al., 2019). For a review of different parcellations see (Eickhoff et al., 2018)), it is advisable to utilize a parcellation that has over 100 nodes, if small-world properties are to be modelled(Hilgetag and Goulas, 2016; Papo et al., 2016).

5.2 DYNAMICAL ANALYSIS OF NETWORKS

Once the network's size and density were analyzed and defined, a dynamical model was imposed on the nodes. This particular model was used previously showing that the chaotic nature of the node(Xu et al., 2018) or moderate amount of noise (Orio et al., 2018) were the main drivers of the network's multistability. In this work, I focused on analyzing how the structure drives multistability, modifying noise and density levels, and node dynamics. The main finding is that latticed (regular) networks showed higher multistability (var(FCD)) than small world or random ones, irrespectively of network's density (fig. 4.3 and supp. figure C.8). This may be explained by the network's modularity. Modularity could be understood as small communities built inside the network. In other words, how many "isolated" subsets may be found in the network (Newman, 2004). High modularity was found on latticed networks ($p = 0{,}00$) and it decreased in random networks ($p = 1{,}00$). Hence, a more modular network contains more communities on which each of them has its own dynamical structure. This leads to a more diverse pattern observed in FCD

and, conversely, a more dynamic FCD. A similar explanation could be made with respect to the network's metastability(supp. fig. C.7).

Additionally, latticed networks are less prone to synchronization, as opposed to the small-world or random ones (fig. 4.3 and supp. fig. C.6). In small-world and random networks, the path length is small, because it is required a few steps for traveling from node a to node b (Watts and Strogatz, 1998). This "proximity" between nodes allows the network to synchronize easier, as compared with networks with high path length, such as regular networks. Therefore, as the average path length diminishes from latticed to random network, they synchronize easily (Barahona and Pecora, 2002; Nishikawa et al., 2003; Percha et al., 2005)

5.3 STRUCTURE-FUNCTION RELATIONSHIP

To determine the structure-function relationship, structural metrics that account for integration(η), segregation(Q, τ or *smallworldness* (ω) were selected. By changing the reconnection probability, i.e., changing the integration-segregation properties of the network, measured by the previous metrics, I explored how dynamically rich a network could be, given its structural parameters. For that, the relationship between functional properties, such as multistability and FCD variance, was related to structural properties.

At first, more segregated networks, i.e. regular networks, showed higher values of dynamics. In other words, segregated networks are "dynamically richer" than random ones (Figures 4.6, 4.7 and supp. figs. C.7, C.8), as previously discussed.

With the linearization shown in figures 4.8 and 4.9, it is possible to establish a link between the structure and function. It was observed that metastability is better explained by efficiency, and multistability (Var(FCD)) is better explained by small world index ω. This result can be summarized as following: **Metastability is better explained by integration properties of the network, while Var(FCD) (a proxy for multistability) is better explained by the small-world index.**

The fact that the integrated properties of the network explain metastability could be

better understood in the light of the definition made by Karl Friston “We have framed metastability in terms of the successive expression of transients that emerge when simulated neural populations are loosely coupled or sparsely connected” (Friston, 1997). Efficiency, in this case, serves as the explanatory variable that is inversely correlated with metastability. High metastability was found on regular networks, where the efficiency is low. On the contrary, low metastability was found in random networks with high efficiency.

On the other hand, multistability is defined by Kelso as the property of a system on which multiple coexisting attractors, but none of them are strong enough to let the system converge to a particular attractor, letting the system wander between states(Kelso, 2012). Why the small-world property of the network explains this particular dynamical phenomenon? Other works have shown a relationship between small-world networks and the existence of multiple attractors (Netoff et al., 2004; Rothkegel and Lehnertz, 2009; Shabunin, 2015). A possible explanation may lie in the balance between the clustering coefficient and path length, which represents the balance between the network’s segregation and integration. A fully integrated network acts as a unit, existing in only one state. On the other side, a fully segregated network has many states, but they seldom communicate with each other, as its path length is very large. Thus, a small-world network shares both characteristics: numerous states, given by its segregated properties, and the ability of those states to communicate to each other, given the short path length of the network.

However, there is still no theoretical or mechanistic explanation for this observed behavior. Further studies that explore analytically the relationship between network structure and network dynamics are needed.

To summarize, the transitions between states (metastability) inversely correlate with the integration properties of the structural network. Dynamical richness, on the other hand, is best explained by an inverse correlation with the balance between integration and segregation, represented by small world parameter ω.

Chapter 6

Conclusion

To summarize, this work consisted of exploring the relationship between structure and function in a biophysically inspired network.

By using a Watts-Strogatz algorithm and changing the reconnection probability, regular, small world, and random networks were built (Watts and Strogatz, 1998). To characterize the network properties, metrics were calculated on these networks. These metrics showed dependence with respect to node number, network density, and reconnection probability(Muldoon et al., 2016; Neal, 2017; Telesford et al., 2011). In particular, the small-world property ω was selected, as it allowed comparison between the three kinds of topologies used. As the brain is not a small world network (Hilgetag and Goulas, 2016; Papo et al., 2016), but instead has small-world properties, it is essential to take into account the three key parameters that define the network (Node number, network density, and reconnection probability), in order to avoid misinterpretations of the small-world properties.

Dynamical richness was higher in regular networks than in small world or random ones. This could be explained by the number of clusters or the segregation that regular networks have. However, regular networks are more difficult to synchronize than small world or regular networks. In turn, this is explained by the path length or the network's integration capacity. Thus, it could be proposed that small-world networks live in these two worlds: rich dynamics and high synchronizability.

Metastability, referred to as states that emerge through interactions of clusters or populations of nodes, is better explained by the segregation properties of the network. The rationale behind this is that a segregated network has more clusters and hence, it is more likely to be metastable. Multistability, defined by the transit between multiples attractors, is better explained by small-world index ω. In this work, only two values of reconnection probability that yield to small-world networks were used ($p = 0{,}05, 0{,}20$). Further analysis within the range of small world, may help us to understand if this relationship is given by the ratio between segregation and integration

in the network.

It should be noticed, however, that fitting the data to an exponential function was only for comparison and visualization purposes. Other functions may offer a better insight into the relationship between structure and function in network dynamics.

References

Arslan, S., Ktena, S. I., Makropoulos, A., Robinson, E. C., Rueckert, D., and Parisot, S. (2018). Human brain mapping: A systematic comparison of parcellation methods for the human cerebral cortex. Neuroimage, 170:5–30.

Barahona, M. and Pecora, L. M. (2002). Synchronization in small-world systems. Physical review letters, 89(5):054101.

Bassett, D. S. and Bullmore, E. (2006). Small-world brain networks. The neuroscientist, 12(6):512–523.

Bassett, D. S. and Bullmore, E. T. (2017). Small-world brain networks revisited. The Neuroscientist, 23(5):499–516.

Batista-García-Ramó, K. and Fernández-Verdecia, C. I. (2018). What we know about the brain structure–function relationship. Behavioral Sciences, 8(4):39.

Berglund, N. and Gentz, B. (2010). Stochastic dynamic bifurcations and excitability. Stochastic methods in Neuroscience, pages 64–93.

Cabral, J., Luckhoo, H., Woolrich, M., Joensson, M., Mohseni, H., Baker, A., Kringelbach, M. L., and Deco, G. (2014). Exploring mechanisms of spontaneous functional connectivity in meg: how delayed network interactions lead to structured amplitude envelopes of band-pass filtered oscillations. Neuroimage, 90:423–435.

Cohen, J. R. and D'Esposito, M. (2016). The segregation and integration of distinct brain networks and their relationship to cognition. Journal of Neuroscience, 36(48):12083–12094.

da Silva, F. L. (2013). Eeg and meg: relevance to neuroscience. Neuron, 80(5):1112–1128.

Deco, G., Jirsa, V., McIntosh, A. R., Sporns, O., and Kötter, R. (2009). Key role of coupling, delay, and noise in resting brain fluctuations. Proceedings of the National Academy of Sciences, 106(25):10302–10307.

Deco, G. and Jirsa, V. K. (2012). Ongoing cortical activity at rest: criticality, multistability, and ghost attractors. Journal of Neuroscience, 32(10):3366–3375.

Deco, G., Tononi, G., Boly, M., and Kringelbach, M. L. (2015). Rethinking segregation and integration: contributions of whole-brain modelling. Nature Reviews Neuroscience, 16(7):430.

Diez, I., Bonifazi, P., Escudero, I., Mateos, B., Muñoz, M. A., Stramaglia, S., and Cortes, J. M. (2015). A novel brain partition highlights the modular skeleton shared by structure and function. Scientific reports, 5:10532.

Dong, D., Duan, M., Wang, Y., Zhang, X., Jia, X., Li, Y., Xin, F., Yao, D., and Luo, C. (2018). Reconfiguration of dynamic functional connectivity in sensory and perceptual system in schizophrenia. Cerebral Cortex.

Eickhoff, S. B., Yeo, B. T., and Genon, S. (2018). Imaging-based parcellations of the human brain. Nature Reviews Neuroscience, 19(11):672–686.

Fornito, A. and Harrison, B. (2012). Brain connectivity and mental illness. Frontiers in psychiatry, 3:72.

Fornito, A., Zalesky, A., and Breakspear, M. (2015). The connectomics of brain disorders. Nature Reviews Neuroscience, 16(3):159.

Fox, M. D., Snyder, A. Z., Vincent, J. L., and Raichle, M. E. (2007). Intrinsic fluctuations within cortical systems account for intertrial variability in human behavior. Neuron, 56(1):171–184.

Friston, K. J. (1997). Transients, metastability, and neuronal dynamics. Neuroimage, 5(2):164–171.

Hagmann, P., Cammoun, L., Gigandet, X., Meuli, R., Honey, C. J., Wedeen, V. J., and Sporns, O. (2008). Mapping the structural core of human cerebral cortex. PLoS biology, 6(7):e159.

Hansen, E. C., Battaglia, D., Spiegler, A., Deco, G., and Jirsa, V. K. (2015). Functional connectivity dynamics: modeling the switching behavior of the resting state. Neuroimage, 105:525–535.

Heitmann, S. and Breakspear, M. (2018). Putting the “dynamic” back into dynamic functional connectivity. Network Neuroscience, 2(02):150–174.

Hilgetag, C. C. and Goulas, A. (2016). Is the brain really a small-world network? Brain Structure and Function, 221(4):2361–2366.

Honey, C., Sporns, O., Cammoun, L., Gigandet, X., Thiran, J.-P., Meuli, R., and Hagmann, P. (2009). Predicting human resting-state functional connectivity from structural connectivity. Proceedings of the National Academy of Sciences, 106(6):2035–2040.

Honey, C. J., Kötter, R., Breakspear, M., and Sporns, O. (2007). Network structure of cerebral cortex shapes functional connectivity on multiple time scales. Proceedings of the National Academy of Sciences, 104(24):10240–10245.

Humphries, M. D. and Gurney, K. (2008). Network ‘small-world-ness’: a quantitative method for determining canonical network equivalence. PloS one, 3(4):e0002051.

Hutchison, R. M., Womelsdorf, T., Allen, E. A., Bandettini, P. A., Calhoun, V. D., Corbetta, M., Della Penna, S., Duyn, J. H., Glover, G. H., Gonzalez-Castillo, J., et al. (2013). Dynamic functional connectivity: promise, issues, and interpretations. Neuroimage, 80:360–378.

Ivanova, A., Zaidel, E., Salamon, N., Bookheimer, S., Uddin, L. Q., and de Bode, S. (2017). Intrinsic functional organization of putative language networks in the brain following left cerebral hemispherectomy. Brain Structure and Function, 222(8):3795–3805.

Kaiser, M. (2011). A tutorial in connectome analysis: topological and spatial features of brain networks. Neuroimage, 57(3):892–907.

Kelso, J. S. (2012). Multistability and metastability: understanding dynamic coordination in the brain. Philosophical Transactions of the Royal Society B: Biological Sciences, 367(1591):906–918.

Laing, C. and Lord, G. J. (2010). Stochastic methods in neuroscience. Oxford University Press.

Latora, V. and Marchiori, M. (2001). Efficient behavior of small-world networks. Physical review letters, 87(19):198701.

Messé, A., Hütt, M.-T., König, P., and Hilgetag, C. C. (2015). A closer look at the apparent correlation of structural and functional connectivity in excitable neural networks. Scientific reports, 5:7870.

Mill, R. D., Ito, T., and Cole, M. W. (2017). From connectome to cognition: The search for mechanism in human functional brain networks. NeuroImage, 160:124–139.

Muldoon, S. F., Bridgeford, E. W., and Bassett, D. S. (2016). Small-world propensity and weighted brain networks. Scientific reports, 6:22057.

Neal, Z. P. (2017). How small is it? comparing indices of small worldliness. Network Science, 5(1):30–44.

Netoff, T. I., Clewley, R., Arno, S., Keck, T., and White, J. A. (2004). Epilepsy in small-world networks. Journal of neuroscience, 24(37):8075–8083.

Newman, M. E. (2004). Fast algorithm for detecting community structure in networks. Physical review E, 69(6):066133.

Nguyen, T. T., Kovacevic, S., Dev, S. I., Lu, K., Liu, T. T., and Eyler, L. T. (2017). Dynamic functional connectivity in bipolar disorder is associated with executive function and processing speed: A preliminary study. Neuropsychology, 31(1):73.

Nishikawa, T., Motter, A. E., Lai, Y.-C., and Hoppensteadt, F. C. (2003). Heterogeneity in oscillator networks: Are smaller worlds easier to synchronize? Physical review letters, 91(1):014101.

Orio, P., Gatica, M., Herzog, R., Maidana, J. P., Castro, S., and Xu, K. (2018). Chaos versus noise as drivers of multistability in neural networks. Chaos: An Interdisciplinary Journal of Nonlinear Science, 28(10):106321.

Orio, P., Parra, A., Madrid, R., González, O., Belmonte, C., and Viana, F. (2012). Role of i h in the firing pattern of mammalian cold thermoreceptor endings. Journal of neurophysiology, 108(11):3009–3023.

Otte, W. M., Van Der Marel, K., Van Meer, M. P., Van Rijen, P. C., Gosselaar, P. H., Braun, K. P., and Dijkhuizen, R. M. (2015). Altered contralateral sensorimotor system organization

after experimental hemispherectomy: a structural and functional connectivity study. Journal of Cerebral Blood Flow & Metabolism, 35(8):1358–1367.

Papo, D., Zanin, M., Martínez, J. H., and Buldú, J. M. (2016). Beware of the small-world neuroscientist! Frontiers in human neuroscience, 10:96.

Park, H.-J. and Friston, K. (2013). Structural and functional brain networks: from connections to cognition. Science, 342(6158):1238411.

Percha, B., Dzakpasu, R., Żochowski, M., and Parent, J. (2005). Transition from local to global phase synchrony in small world neural network and its possible implications for epilepsy. Physical Review E, 72(3):031909.

Preti, M. G., Bolton, T. A., and Van De Ville, D. (2017). The dynamic functional connectome: State-of-the-art and perspectives. Neuroimage, 160:41–54.

Rodriguez, A. and Laio, A. (2014). Clustering by fast search and find of density peaks. Science, 344(6191):1492–1496.

Rothkegel, A. and Lehnertz, K. (2009). Multistability, local pattern formation, and global collective firing in a small-world network of nonleaky integrate-and-fire neurons. Chaos: An Interdisciplinary Journal of Nonlinear Science, 19(1):015109.

Rubinov, M. and Sporns, O. (2010). Complex network measures of brain connectivity: uses and interpretations. Neuroimage, 52(3):1059–1069.

Schumacher, J., Peraza, L. R., Firbank, M., Thomas, A. J., Kaiser, M., Gallagher, P., O'Brien, J. T., Blamire, A. M., and Taylor, J.-P. (2019). Dynamic functional connectivity changes in dementia with lewy bodies and alzheimer's disease. NeuroImage: Clinical, page 101812.

Shabunin, A. (2015). Phase multistability in a dynamical small world network. Chaos: An Interdisciplinary Journal of Nonlinear Science, 25(1):013109.

Sporns, O. (2013). Network attributes for segregation and integration in the human brain. Current opinion in neurobiology, 23(2):162–171.

Sporns, O., Tononi, G., and Kötter, R. (2005). The human connectome: a structural description of the human brain. PLoS computational biology, 1(4):e42.

Szalkai, B., Kerepesi, C., Varga, B., and Grolmusz, V. (2019). High-resolution directed human connectomes and the consensus connectome dynamics. PloS one, 14(4):e0215473.

Telesford, Q. K., Joyce, K. E., Hayasaka, S., Burdette, J. H., and Laurienti, P. J. (2011). The ubiquity of small-world networks. Brain connectivity, 1(5):367–375.

Tian, L., Li, Q., Wang, C., and Yu, J. (2018). Changes in dynamic functional connections with aging. Neuroimage, 172:31–39.

Uddin, L. Q. (2013). Complex relationships between structural and functional brain connectivity. Trends in cognitive sciences, 17(12):600–602.

Van den Heuvel, M. P., Bullmore, E. T., and Sporns, O. (2016). Comparative connectomics. Trends in cognitive sciences, 20(5):345–361.

Van Den Heuvel, M. P. and Pol, H. E. H. (2010). Exploring the brain network: a review on resting-state fmri functional connectivity. European neuropsychopharmacology, 20(8):519–534.

Van Wijk, B. C., Stam, C. J., and Daffertshofer, A. (2010). Comparing brain networks of different size and connectivity density using graph theory. PloS one, 5(10):e13701.

Watts, D. J. and Strogatz, S. H. (1998). Collective dynamics of 'small-world'networks. nature, 393(6684):440.

Xu, K., Maidana, J. P., Castro, S., and Orio, P. (2018). Synchronization transition in neuronal networks composed of chaotic or non-chaotic oscillators. Scientific reports, 8(1):8370.

Xu, T., Cullen, K. R., Mueller, B., Schreiner, M. W., Lim, K. O., Schulz, S. C., and Parhi, K. K. (2016). Network analysis of functional brain connectivity in borderline personality disorder using resting-state fmri. NeuroImage: Clinical, 11:302–315.

Yger, P., Spampinato, G. L., Esposito, E., Lefebvre, B., Deny, S., Gardella, C., Stimberg, M., Jetter, F., Zeck, G., Picaud, S., et al. (2018). A spike sorting toolbox for up to thousands of electrodes validated with ground truth recordings in vitro and in vivo. Elife, 7:e34518.

Zhi, D., Calhoun, V. D., Lv, L., Ma, X., Ke, Q., Fu, Z., Du, Y., Yang, Y., Yang, X., Pan, M., et al. (2018). Aberrant dynamic functional network connectivity and graph properties in major depressive disorder. Frontiers in psychiatry, 9.

Appendix A

Dynamical model

A.1 GENERAL MODEL

The implemented model was used previously by our laboratory (Orio et al., 2018). This model is a modified Huber & Braun, that incorporates an additional hyperpolarization activating current (I_h), which allows controlling the slow oscillation period. The dynamic of each node is governed by the following dynamics

$$C_m\dot{V} = -i_{sd} - i_d - i_{sr} - i_r - i_h - i_l - I_{syn} \tag{A.1}$$

Here, C_m is the membrane capacitance, V is the membrane voltage. Changes in the voltage are driven by a slow Na_p/Ca_T depolarizating (i_{sd}), slow depolarizing Na_v (i_d), slow repolarizing K_{Ca} (i_{sr}), repolarizing K_{dr} (i_r), hyperpolarizing (i_h), leak (i_l) and synaptic (I_{syn}) currents.

A Currents

The currents could be expresed as

$$i_x = \rho g_x a_x (V - E_x), \;\; x = sd, d, r, h, l \tag{A.2}$$

Here, g_x corresponds to the maximal conductance density for each ion current. a_x represents the probability of the open channels for certain ion ($a_l = 1$). E_x is the reversal potential for each current. ρ is a temperature-dependent factor for the ionic current.

The probability for a channel to be open is represented as

$$\dot{a_x} = \phi \frac{a_x^\infty - a_x}{\tau_x}, \;\; x = sd, r, h \tag{A.3}$$

and

$$a_x^\infty = \frac{1}{1 + \exp[-z_x(V - V_x^0)]} \tag{A.4}$$

In here, z_x is the slope of the activation function, V_x^0 is the voltage for the half-activation and ϕ is a temperature dependent function for ion channel kinetics.

The slow repolarizing current i_{sr} is expresed as

$$i_{sr} = \rho g_{sr} p_{sr} (V - E_{sr}) \tag{A.5}$$

$$p_{sr} = \frac{a_{sr}^2}{a_{sr}^2 + 0{,}4^2} \tag{A.6}$$

In here, ρ, g_{sr}, E_{sr} corresponds to the temperature-dependent, maximal conductance and reversal potential for the ion, as previous currents, however, a_{sr} represents the intracellular calcium concentration and is defined as

$$\dot{a_{sr}} = \phi \frac{-\eta i_{sd} - \kappa a_{sr}}{\tau_{sr}} \tag{A.7}$$

where η, κ represents the factor that relates the increase in calcium concentration and the rate of calcium decrease, respectively.

Finally

$$a_d = a_d^\infty = \frac{1}{1 + \exp[-z_d(V - V_d^0)]} \tag{A.8}$$

B Temperature

The temperature functions are defined as

$$\rho = 1{,}3^{(0{,}1T-2{,}5)} \quad \phi = 3^{(0{,}1T-2{,}5)} \tag{A.9}$$

where T corresponds to temperature in Celsius.

C Synaptic current

Synaptic currents are modeled as driven by electrical synapses between two nodes j, k.

$$I_{syn,k} = \sum_{j=1, j\neq k}^{N} C_{jk} g_{jk} (V_j - V_k) \tag{A.10}$$

In here, C_{jk} is the j,k element of the connectivity matrix used for the topology. If the nodes j,k are connected, then $C_{j,k} = C_{k,j} = 1$, otherwise the element is 0. The synaptic conductance g_{jk} was set equal for every pair j,k, leading to $g_{j,k} = g$.

A.2 STOCHASTIC SIMULATION

Stochastic simulation was conducted as previously reported (Orio et al., 2018). Stochastic opening and closing for ionic channels that drive the subthreshold oscillation (sd, sr, h) were added in the form of diffusion approximation (Orio et al., 2018). Hence, the stochastic equations for a_{sd}, a_h were implemented as the following

$$\dot{a_i} = \phi\frac{a_i^\infty - a_i}{\tau_i}dt + \sqrt{\phi\frac{|a_i|(1-a_i^\infty) + a_i^\infty(1-|a_i|)}{N_i\tau_i}}dW_t \quad i = sd, h \tag{A.11}$$

N_i is the number of channels, and W is a Wiener process. Thus $dW_t \sim \mathcal{N}(0,1)$

Due that i_{sr} is expressed by calcium concentrations and not by channel opening, the noise factor was introduced into the current term:

$$i_{sr} = \rho g_{sr}(V - E_{sr})\left(p_{sr} + \sqrt{\frac{p_{sr}(1-p_{sr}}{N_{sr}}}\xi(t)\right) \tag{A.12}$$

p_{sr} is the same parameter as equation A.6,N_{sr} corresponds to number of channels, and $\xi(t) \sim \mathcal{N}(0,1)$

A.3 NOISE CONTROL

In the previous section, the stochastic noise equations that were used in the model are inversely proportional with respect to the channel number N. Also, N is defined as

$$N_i = 10\frac{g_i A}{g_i^u} \quad i = sd, h, sr \tag{A.13}$$

where g_i is the conductance density in mS/cm^2, A is the neuron membrane area in m^2, and g_i^u

is the total channel conductance in $pS/channel$. It may be observed that the noise level is then modulated by the area. Low area mean more channels in the membrane and thus, more noise.

Appendix B

Parameters

Parameter	Value	Description
g_d	2.5	depolarizing conductance
g_r	2.8	repolarizing conductance
g_{sd}	0.21	slow depolarizing conductance
g_{sr}	0.28	slow repolarizing conductance
g_l	0.06	leak conductance
g_h	0.4	hiperpolarization conductance
$V_d(0)$	-25	depolarizing initial voltage
$V_r(0)$	-25	repolarization initial voltage
s_d	0.25	activation slope for depolarizing activation particle
s_r	0.25	activation slope for repolarizing activation particle
t_r	2	repolarization time constant for activation particle
$V_{sd}(0)$	-40	slow depolarization initial voltage
s_{sd}	0.11	activation slope for slow depolarizing activation particle
t_{sd}	10	slow depolarization time constant for activation particle
η	0.014	current increase by calcium increase factor
κ	0.18	calcium decrease factor
t_{sr}	35	slow repolarization time constant for activation particle
$V_h(0)$	-85	hiperpolarization initial voltage
s_h	-0.14	activation slope for hiperolarizing activation particle
t_h	125	hiperpolarization time constant for activation particle
Ed	50	reversal potential for depolarization conductance
Er	-90	reversal potential for repolarization conductance
El	-80	reversal potential for leak conductance
Eh	-30	reversal potential for hiperpolarization conductance
g^u_{sd}	20	slow depolarization conductance per channel
g^u_{sr}	20	slow repolarization conductance per channel
g^u_h	2	slow hiperpolarization conductance per channel
temperature	36	working temperature for neurons
nodes	250	number of nodes present in the network
adaptTime	30000	adaptation time for transient removal.
adaptInt	0.05	dt for transient removal
runInt	0.05	dt for stochastic simulation
sampling	0.25	sampling rate for storing voltage trace
cutfreq	50	low pass filter cut frequency
decimate	20	subsampling factor after filtering

TABLE B.1: Summary of parameters and values used in this work

Appendix C

Supplementary Figures

C.1 SMALL WORLD METRICS

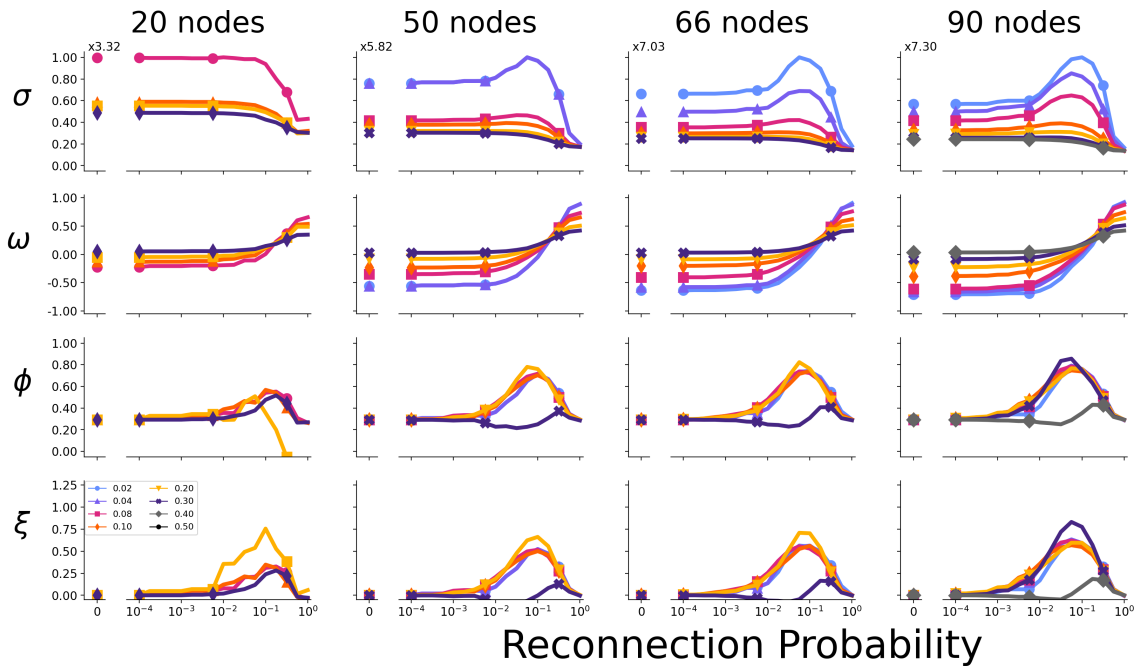

FIGURE C.1: **Small world metrics for networks with 20-90 nodes.**

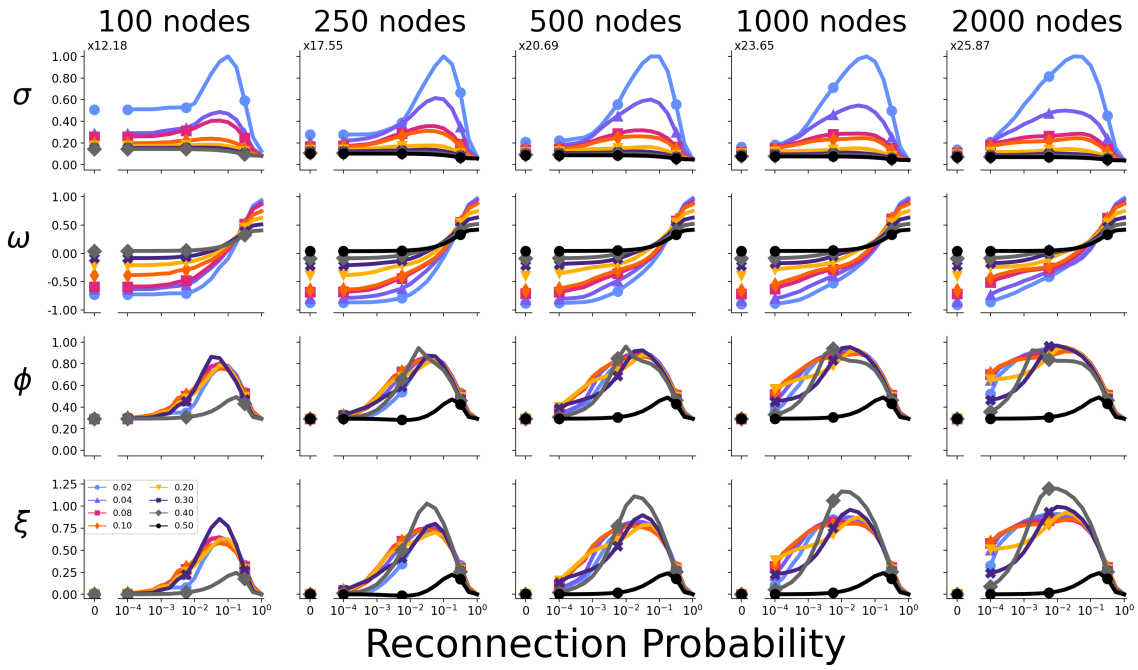

FIGURE C.2: **Small world metrics for networks with 100-2000 nodes.** For networks with different densities and node number, small world metrics were calculated. Observe that densities over 50 % are achievable for networks with 50 or more nodes.

C.2 NETWORK METRICS

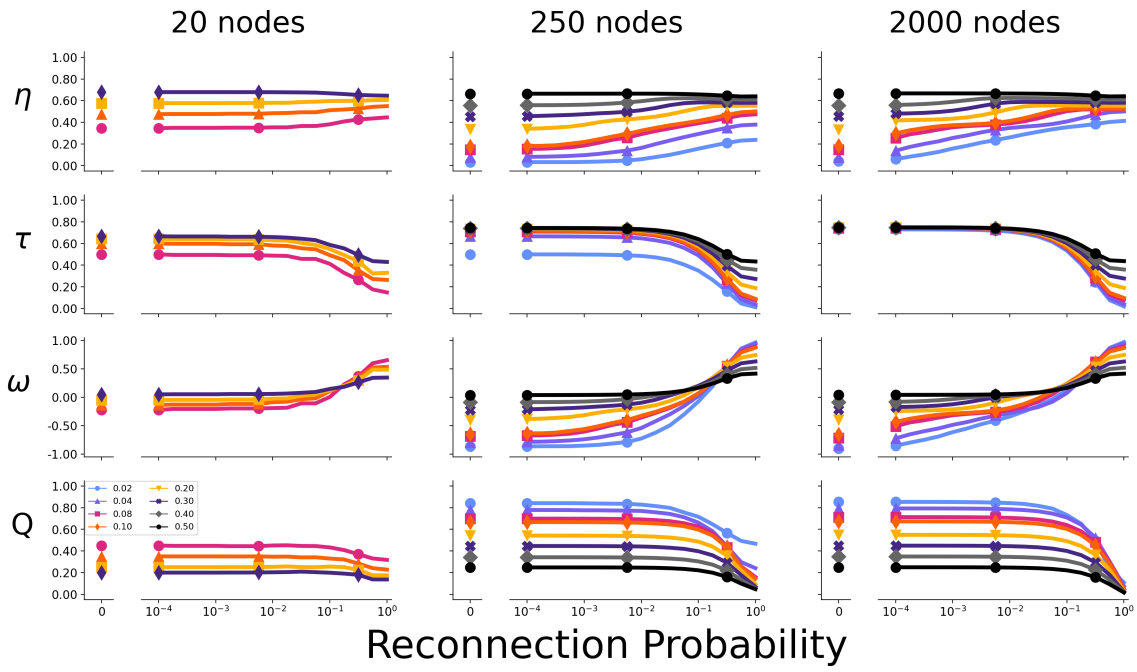

FIGURE C.3: **Integration and segregation metrics under different network size and network density.**

C.3 FCD FOR DIFFERENT DENSITIES

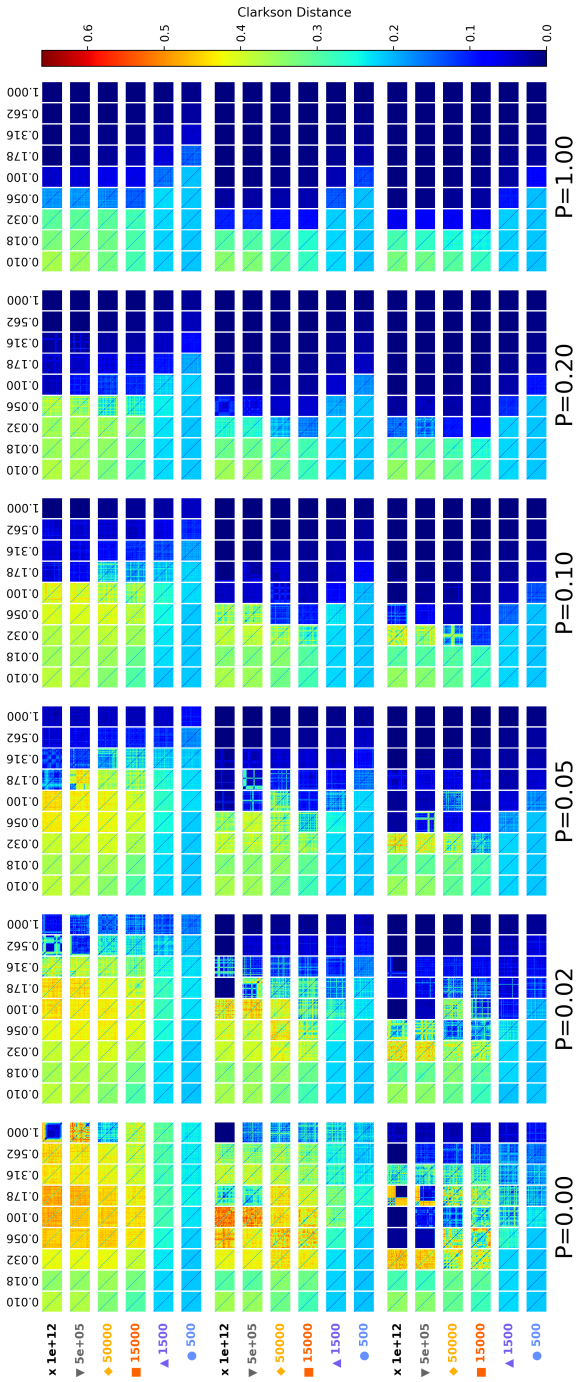

FIGURE C.4: **FCD changes with respect to density and reconnection probability.** FCDs for different reconnection probabilities (columns) or network density (rows, $2, 4, 8\,\%$ are shown. Each combination of noise and coupling corresponds to one FCD. Noise labels and colors are the same as figure 4.3.

C.4 DYNAMIC METRICS FOR DIFFERENT NETWORK'S DENSITIES

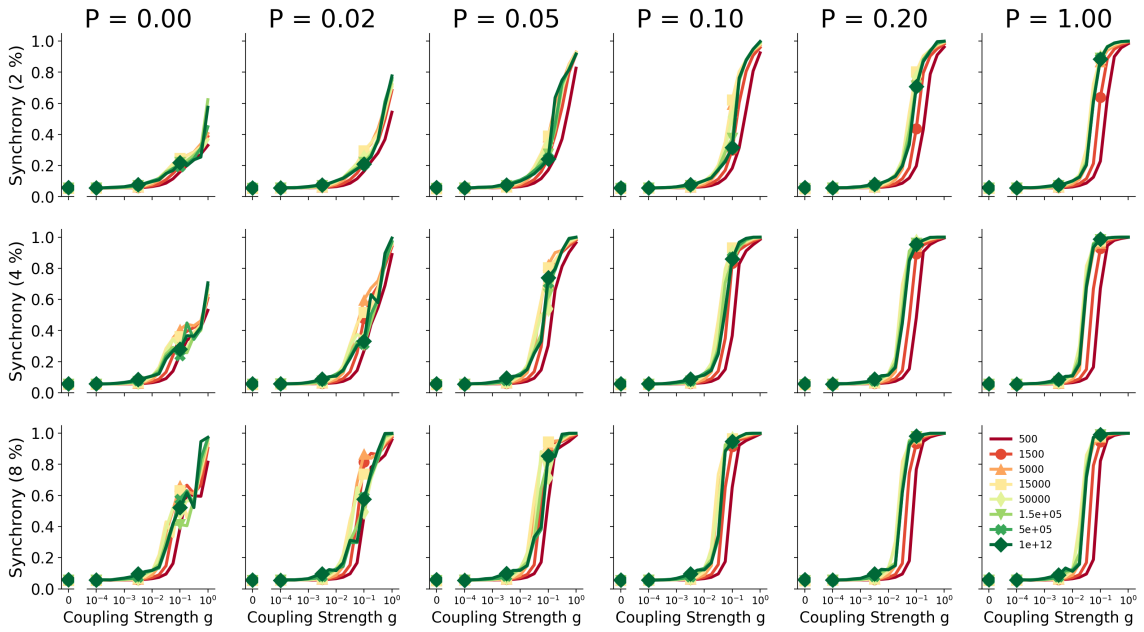

FIGURE C.5: **Synchronization for different densities and reconnection probability.** Each color represents noise levels. Green traces are low noises while red traces represents high noise. Notice that as density is increased (rows), full synchronization is achieved at lower reconnection probabilities. Each point corresponds to the average of four realizations. For visualization purposes, only 3 points over 18 are marked.

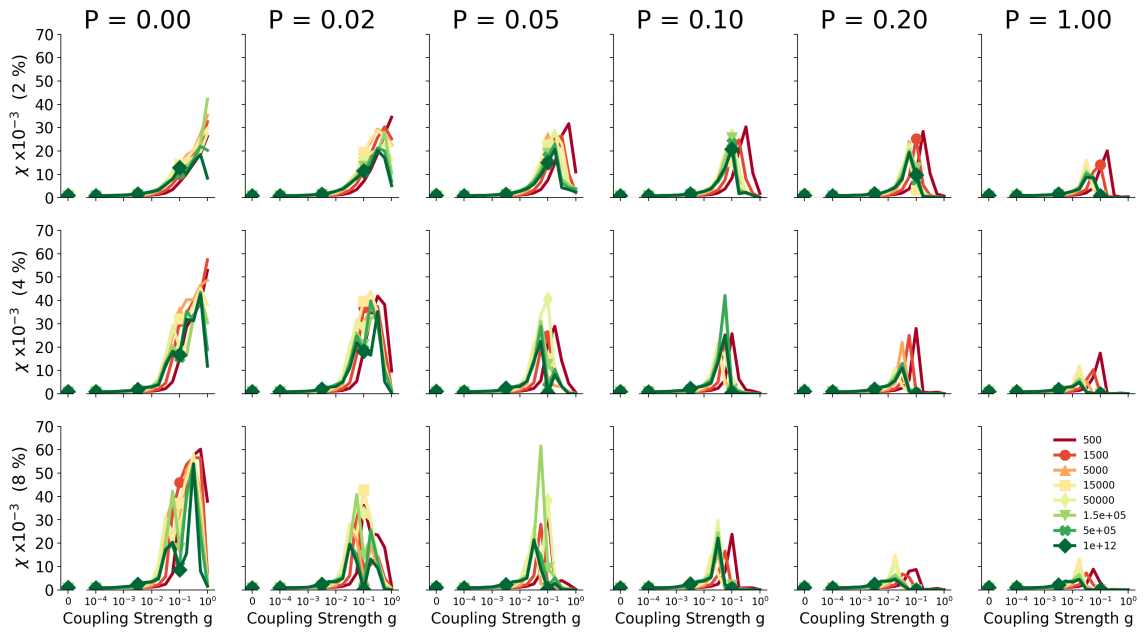

FIGURE C.6: **Multistability for different densities and reconnection probability.** Each color represents noise levels. Green traces are low noises while red traces represents high noise. Notice that as density is increased (rows), multistability decreases. Each point corresponds to the average of four realizations. For visualization purposes, only 3 points over 18 are marked.

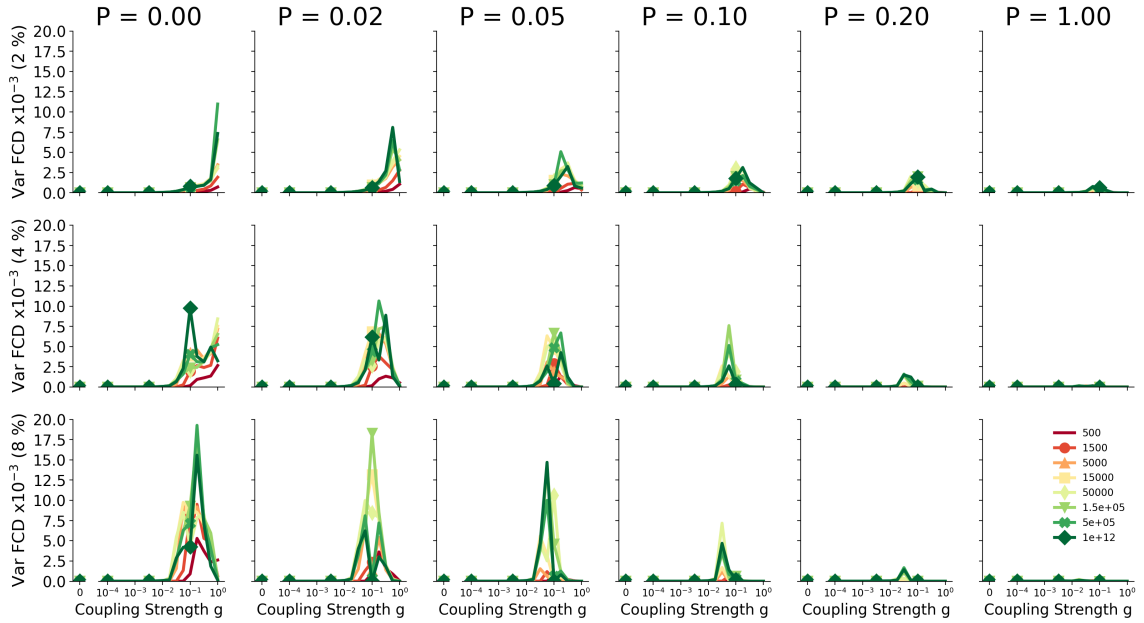

FIGURE C.7: **Metastability for different densities and reconnection probability.** Each color represents noise levels. Green traces are low noises while red traces represents high noise. Each point corresponds to the average of four realizations. For visualization purposes, only 3 points over 18 are marked.

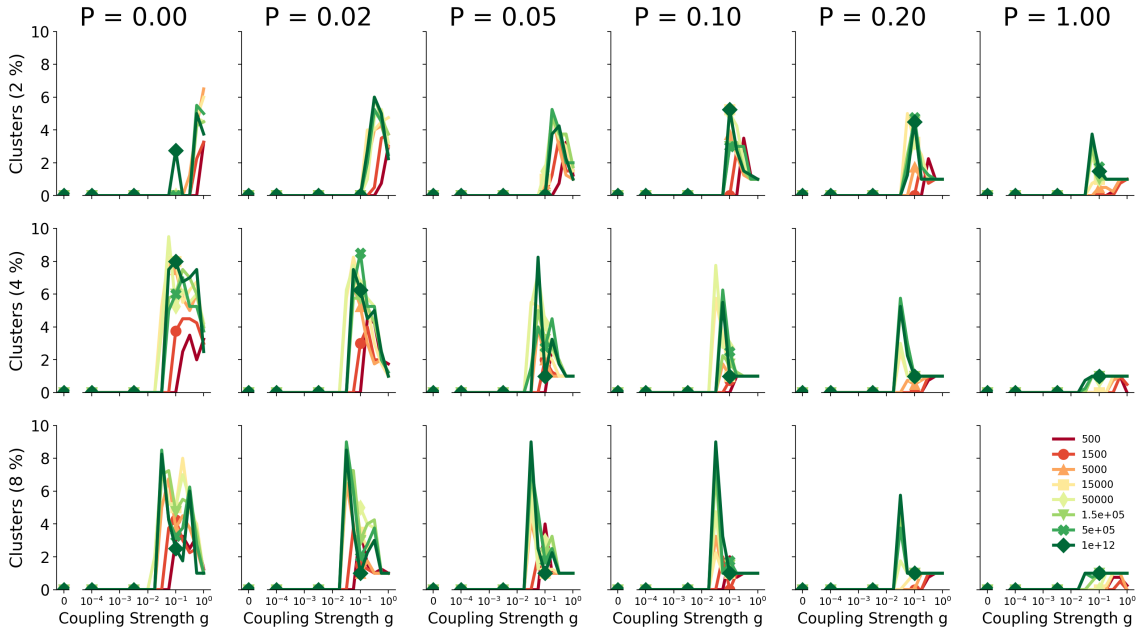

FIGURE C.8: **Cluster or states for different densities and reconnection probability.** Each color represents noise levels. Green traces are low noises while red traces represents high noise. Clusters were identified by clustering algorigthm and PCA projection (see methods). As Var(FCD), increasing the reconnection probability tends to decrease the states or clusters found. Each point corresponds to the average of four realizations. For visualization purposes, only 3 points over 18 are marked.